



1 **Wintertime Aerosol Measurements during the Chilean Coastal Orographic**

2 **Precipitation Experiment**

3

4 Sara Lynn Fuels ¹

5 Adam K. Massmann ²

6 Aldo Montecinos ³

7 Elisabeth Andrews ^{4,5}

8 David E. Kingsmill ⁵

9 Justin R. Minder ²

10 René D. Garreaud ⁶

11 Jefferson R. Snider ^{1,7}

12

13 ¹ University of Wyoming, Laramie, WY

14

15 ² University at Albany, Albany, NY

16

17 ³ Universidad de Concepción, Concepción, Chile

18

19 ⁴ NOAA ESRL Global Monitoring Division, Boulder, CO

20

21 ⁵ University of Colorado, Boulder, CO

22

23 ⁶ Universidad de Chile, Santiago, Chile

24

25 ⁷ Corresponding Author



26 **Abstract**

27 The Chilean Coastal Orographic Precipitation Experiment (CCOPE) was a three-month
28 field campaign (June, July and August 2015) that investigated wintertime coastal rain events.
29 Reported here are analyses of aerosol measurements made at a coastal site during CCOPE. The
30 aerosol monitoring site was located near Arauco, Chile. Aerosol number concentrations and
31 aerosol size distributions were acquired with a Condensation Particle Counter (CPC) and an
32 Ultra High Sensitivity Aerosol Spectrometer (UHSAS). Arauco CPC concentrations were
33 compared to those measured at the NOAA observatory Trinidad Head (THD) on the North
34 Pacific Coast of California. The winter averaged CPC concentration at Arauco is $2971 \text{ cm}^{-3} \pm$
35 1802 cm^{-3} ; at THD the average is $1059 \text{ cm}^{-3} \pm 855 \text{ cm}^{-3}$. Despite the typically more pristine
36 Southern Pacific region, the Arauco average is larger than at THD ($p < 0.01$). Aerosol size
37 distribution measurements acquired during episodes of onshore flow were analyzed with Köhler
38 theory and used to parameterize cloud condensation nuclei activation spectra. In addition, sea
39 salt aerosol (SSA) concentration was parameterized as a function of sea surface wind speed. It is
40 anticipated these parameterizations will be applied in modeling of wintertime Chilean coastal
41 precipitation.

42



43 1 Introduction

44 Forecast error due to incomplete understanding of atmospheric aerosols is evident in the
45 predictions of many atmospheric models. As an example, general circulation models (GCMs) are
46 used to forecast the Earth system's response to emissions of both aerosols and greenhouse gases.
47 In spite of several decades of GCM development, the effect of aerosols on future climate remains
48 uncertain (Boucher et al. 2013), particularly when compared to the greater certainty in climate
49 forcing from anthropogenic greenhouse gases (e.g., Hansen 2009, his Fig. 10).

50 Aerosols perturb the abundance of cloud droplets and rain drops within clouds warmer
51 than 0 °C (liquid-only clouds). Via this interaction, both upward reflection of solar radiation by
52 cloud cover (Albrecht 1989), and upward reflection by individual cloud elements (Twomey
53 1974) increase with increased aerosol abundance. Commonly referred to as aerosol indirect
54 effects on climate, these processes decrease the amount of solar energy absorbed by the Earth
55 system, and thus oppose global warming due to greenhouse gases. Other aerosol indirect effects,
56 for example those due to aerosols nucleating ice in mixed-phase clouds (McCoy et al., 2014),
57 augment greenhouse gas warming.

58 Because of its lower population and lower intensity of anthropogenic aerosol emissions,
59 the Southern Hemisphere has been explored as a region for conducting studies of aerosol indirect
60 effects and for exploring contrasts with the Northern Hemisphere (Schwartz, 1988; Gras, 1990;
61 Gras 1995; Yum and Hudson 2004). This study contributes to those previous wintertime
62 investigations of Southern Hemispheric aerosols. We emphasize the following topics: 1) The
63 parameterized relationship between sea salt aerosol (SSA) concentration and sea surface wind
64 speed; 2) The concentration of aerosol particles that are both smaller and more numerous than
65 the SSA, and their role as cloud condensation nuclei (CCN); 3) The parameterized relationship



66 describing CCN activation spectra (Rogers and Yau, 1989; chapter 6), and 4) the potential
67 application of the SSA and CCN parameterizations in numerical modelling of wintertime
68 Southern Hemispheric clouds and precipitation. Motivating our investigation are modeling
69 studies (Feingold et al. 1999), and analyses of field measurements (Gerber and Frick 2012),
70 indicating that the reduction of rainfall due to increased CCN can be negated by SSA particles.

71 Measurements made with a Condensation Particle Counter (CPC), an instrument that
72 reports the concentration of particles with diameter (D) larger than $\sim 0.01 \mu\text{m}$, have formed the
73 basis of many previous investigations of aerosol abundance (Gras 1990; Brechtel et al. 1998;
74 Dall'Osto et al. 2009; Andreae 2009). These studies also evaluated air parcel back trajectories
75 and demonstrated that marine source regions are characterized by distinctly smaller CPC
76 concentrations than continental regions. Measurements of aerosol size distributions (ASDs) can
77 also aid understanding of the contrast between marine and continental CPC concentrations
78 (Brechtel et al. 1998; Birmili et al. 2001; Raes et al. 1997). The latter studies investigated
79 accumulation mode particles, centered at $\sim 0.1 \mu\text{m}$, and particles sizing in a mode at a distinctly
80 smaller central diameter ($\sim 0.05 \mu\text{m}$). This smaller mode is commonly referred to as the Aitken
81 mode. In marine settings, the coexistence of both modes has been attributed to in-cloud
82 conversion of gas-phase sulfur dioxide (SO_2) to aerosol-phase sulfate (Hoppel et al. 1994), to
83 coalescence scavenging occurring within clouds (Hudson et al. 2015), and to new particle
84 formation (Covert et al. 1992; Petters et al. 2006). The latter process occurs in environments with
85 sufficiently enhanced ratios of SO_2 relative to aerosol.

86 The present work is an analysis of CPC concentrations and ASDs measured at a coastal
87 site on the Central Chilean Pacific coast during the Southern Hemisphere winter (June, July, and
88 August). Aerosol measurements were made during the Chilean Coastal Orographic Precipitation



89 Experiment (CCOPE) of 2015. CCOPE investigated aerosol properties and coastal orographic
90 precipitation and meteorology (Massmann et al. 2017).

91 This paper is organized into the following sections: Section 2 has descriptions of the
92 aerosol and meteorological instruments used to make surface measurements during CCOPE, and
93 Sect. 3 describes our analysis methods. Section 4 includes four topics: 1) Analysis of CPC
94 measurements and comparison to Coastal North Pacific measurements, 2) development of a
95 relationship between size-integrated aerosol concentration and size-integrated aerosol volume,
96 and comparison to similar relationships derived for summertime stratocumulus regimes, 3)
97 development of a parameterization of CCN activation spectra, and 4) development of a
98 parameterization of SSA number concentration. In Sect. 5, we compare our findings to previous
99 work, and in Sect. 6 we conclude with an outlook for how our parameterizations could be applied
100 in modeling of wintertime Central Chilean Pacific coast clouds and precipitation.

101 **2 Measurements**

102 **2.1 Measurement Site**

103 During CCOPE, a CPC (model 3010; TSI 2000a) and an Ultra High Sensitivity Aerosol
104 Spectrometer (UHSAS) (DMT 2013) were operated at a residence (37.25° S, 73.34° W, 55 m
105 above mean sea level (MSL)) near Arauco, Chile (population 35,000). Arauco is a coastal town
106 on the Central Chilean Pacific coast. Our measurement site, hereafter the Arauco Site (Fig. 1),
107 was selected because of our aim to characterize aerosols advecting onto South America from the
108 Southeast Pacific. Related to this, our measurements were coordinated with investigations of
109 rainfall inside the domain portrayed in Fig. 1. This study region lies in the South Pacific winter
110 storm track and rainfall here can be strongly enhanced by the Nahuelbuta Mountains (Garreaud



111 et al. 2016; Massmann et al. 2017). During CCOPE, several rainfall events were studied using
112 profiling radars and a precipitation disdrometer deployed at Curanilahue (Fig. 1), and a network
113 of precipitation gauges. The Arauco Site is located on a forested hill; most of the population of
114 Arauco lives east of the Arauco Site at an elevation less than 20 m MSL.

115 Salient characteristics of the CPC and UHSAS are provided in Table 1. These
116 instruments were operated inside the residence at the Arauco Site. In addition, a 3-meter
117 meteorological tower was deployed adjacent to the residence. Thermodynamic state (i.e., T , P ,
118 and humidity) and horizontal wind speed and direction were measured on the tower. CPC and
119 meteorological measurements (minus wind direction) were acquired from 29 May to 14 August
120 (Table 1), UHSAS measurements were acquired from 29 May to 28 June (Table 1), and wind
121 direction measurements were acquired from 19 June to 14 August.

122 2.2 Instrumentation

123 Here we discuss characteristics of the CPC and UHSAS, sampling of the ambient
124 CCOPE aerosol, data acquisition of CPC and UHSAS measurements during CCOPE, and use of
125 the recorded UHSAS histograms to calculate ASDs. Additional information about the UHSAS is
126 provided in Appendix A. In that appendix we discuss how we validated, in a laboratory, the
127 UHSAS's determination of test aerosol concentration and particle size. During those validation
128 studies we intentionally dried the test aerosols to a relative humidity (RH) $\leq 15\%$. Consequently,
129 the effect of aerosol-bound water on either the physical size or the refractive index of the test
130 particles was negligible. UHSAS sizing of partially dried haze droplets ($RH \leq 60\%$), sampled
131 from the ambient atmosphere during CCOPE, and an associated particle size overestimate, is
132 also discussed in Appendix A. In Appendix A, we estimate the particle size overestimate to be \sim
133 20 %.



134 During CCOPE, the CPC and UHSAS sampled ambient aerosol through a section of
135 copper tube (length = 3 m, inner diameter = 0.003 m, volumetric flow rate = $34 \text{ cm}^3 \text{ s}^{-1}$). The
136 inlet end of the tube (hereafter, the sample tube) was secured below an eave on the west side of
137 the residence at the Arauco Site. The Reynolds number (Re) of the flow within the sample tube
138 was 960 and thus well below the value ($Re = 2300$) where laminar flow changes to turbulent
139 flow. Particle transmission efficiencies were evaluated using Eq. (7.29) in Hinds (1999). These
140 are 78% for $D = 0.01 \text{ }\mu\text{m}$ particles and $\geq 99\%$ for $D = 0.1 \text{ }\mu\text{m}$ and $D = 1 \text{ }\mu\text{m}$ particles.

141 The CPC counts particles larger than $D = 0.010 \text{ }\mu\text{m}$ (Table 1)¹ by detecting scattering
142 produced when aerosol particles are drawn through light emitted by a solid state laser ($\lambda = 0.78$
143 μm). Prior to detection, the particle diameter is increased by at least a factor of 10 via alcohol
144 condensation. The aerosol sample flowrate in the CPC was $16 \text{ cm}^3 \text{ s}^{-1}$. The CPC can detect a
145 maximum concentration of $10,000 \text{ cm}^{-3}$. During CCOPE, CPC concentrations were recorded
146 once per second and once every 10 seconds (Table 1).

147 The UHSAS measures scattering produced when aerosol particles are drawn through
148 light emitted by a solid state laser ($\lambda = 1.05 \text{ }\mu\text{m}$). By reference to a calibration table (Cai et al.
149 2008; Cai et al. 2013), the UHSAS microprocessor converts scattered light intensity to particle
150 size and accumulates the derived sizes in a 99 channel histogram. Channel widths are
151 logarithmically uniform ($\Delta \log_{10} D = 0.013$) over the instrument's full range ($0.055 < D < 1.0$
152 μm). During CCOPE, the aerosol sample flow in the UHSAS was controlled at $0.34 \text{ cm}^3 \text{ s}^{-1}$.

153 Eq. (1) was used to calculate the ASD.

¹ The CPC minimum detectable diameters we report are in fact diameters that a CPC detects particles with efficiency = 50 %. The CPC detection efficiency is a steep function of particle diameter (TSI 1996).



$$154 \quad \left(\frac{dN}{d \log_{10} D} \right)_i = \frac{\Delta n_i}{\dot{V} \cdot \Delta t \cdot \Delta \log_{10} D} \quad (1)$$

155 Here Δn_i is the “i th” component of the count histogram and \dot{V} is the aerosol flowrate. During
156 CCOPE, the UHSAS aerosol flow rate and the particle count histogram were recorded once
157 every ten seconds (Table 1), and hence, the sample interval (Δt in Eq. (1)) is 10 s.

158 3 Analysis

159 3.1 Air Mass Classification and Air Parcel Trajectories

160 Locations close to the Arauco Site are shown in Fig. 1. A significant pollution source in
161 the region is the Arauco paper mill which releases 600 ton/yr of SO₂ (Arauco Woodpulp 2010).
162 When winds had an easterly component, the paper mill may have affected air quality at the
163 Arauco Site. Other pollution sources are Curanilahue (population 32,000) and Concepción
164 (population 950,000; this includes several municipalities adjacent to Concepción). In addition,
165 many residences in the region, including the residence where we operated the CPC and UHSAS,
166 burn wood for residential heating.

167 In a subsequent section, we compare CPC concentrations from the Arauco Site to values
168 measured at NOAA’s Trinidad Head (THD) observatory in Northern California (41.05° N, 124.2°
169 W, 107 m MSL). The THD dataset includes contamination from local sources (e.g., campfires lit
170 by day visitors at the Trinidad State Beach Picnic Ground). Additionally, McKinleyville, CA
171 (population 15,000) and Arcata, CA (population 18,000) are the two coastal population centers
172 reasonably close to THD. Both are southeast of the THD, at distances between 15 and 25 km.
173 Northern California’s large population centers (San Francisco Bay Area and Sacramento) are ~
174 300 km southeast of the THD. An important distinction between the sampling at THD and



175 Arauco is the above ground level (a.g.l.) height of the aerosol inlets. This is 10 and 2 m a.g.l. at
176 THD and Arauco, respectively.

177 Wind measurements made at the Arauco Site (Sect. 2.1) and the THD were used to
178 conditionally sample the CPC measurements. At Arauco, wind directions from 180° to 330°
179 were chosen as the clean sector. At THD, the clean sector was chosen from 210° to 360°. The
180 clean sectors at Arauco and THD are shown in Fig. 2. Three factors entered into our selection of
181 the clean sectors: 1) Inclusion of winds from either true south (Arauco Site) or true north (THD),
182 2) the same range of angles (150°) at both sites, and 3) exclusion of wind from the directions of
183 regional population centers.

184 Additionally, we used HYSPLIT back trajectories (NOAA 2016) to conditionally sample
185 Arauco Site aerosol measurements associated with onshore-moving air. The back trajectories
186 were initialized at 00, 06, 12, and 18 UTC. In addition to these static arrival times, trajectories
187 were calculated with the coordinates of the Arauco Site ² and with wind fields from the Global
188 Data Assimilation System. The spatial resolution of the wind data is 0.5°. Position along a
189 trajectory was evaluated hourly. Trajectories that were over the ocean continuously for three
190 days before landfall, and had a direction within the clean sector one hour before arriving at
191 Arauco, were classified as “onshore” trajectories. There are 20 onshore trajectories that overlap
192 with the availability of CCOPE UHSAS measurements.

193 In subsequent sections, a set of 20 two-hour data segments, centered on the onshore
194 trajectory arrival times, are further analyzed. Appendix B describes the numerical filter we used
195 to derive the aerosol properties analyzed in Sect. 4.2, 4.3, 4.4, and 4.5. The filter attenuates
196 aerosol property variability occurring on time scales shorter than 100 s. We developed the filter

² Trajectory starting altitude was set at 60 m MSL (5 m above the Arauco site)



197 to remove narrow “spikes” in the concentration sequences (CPC and UHSAS) which seem to
198 have originated from local sources of aerosol pollution. The Supplementary Material has plots of
199 filtered aerosol properties corresponding to each of the 20 two-hour segments. Four of these
200 were impacted aerosol variability at scales larger than 100 s. In general, these features were not
201 attenuated by the numerical filter. In these instances we discarded (subjectively) portions of the
202 two-hour segment and retained a subset for the analyses conducted in Sect. 4.3, 4.4 and 4.5.

203 Trajectory altitude is important for determining the presence of SSA particles. Onshore
204 trajectories originating from relatively close to the sea surface, and thus classified as onshore
205 “sea surface” trajectories, were required to have pressures > 980 hPa over their three-day
206 advection to the Arauco Site. Eighteen of the 20 onshore trajectories were also sea surface
207 trajectories. An example of a sea surface trajectory is shown in Figs. 3a - b. The sea surface wind
208 speed (U), analyzed in Sect. 4.5, is the average of the six hourly trajectory speeds in the six-hour
209 window ending six hours before the trajectory arrived at the Arauco site. The averaging interval
210 is shown in Fig. 3b. Two onshore trajectories, classified as “aloft”, had pressures substantially
211 smaller than 980 hPa over their three-day advection to the Arauco Site.

212 3.2 Sea Salt Aerosol

213 Correlated values of SSA concentration and sea surface wind speed are reported in many
214 publications. In a review of the topic, Lewis and Schwartz (2004; hereafter LS04) used a
215 particle’s deliquesced wet size, evaluated at 80% relative humidity, to group SSA particles into
216 three size classes. In field studies conducted at a coastal site, Clarke et al. (2003) demonstrated
217 that particles sizing in the middle of LS04’s small particle size class - those with a dry diameter
218 larger than 0.5 μm or a RH = 80% wet diameter larger than 1 μm – had a composition that was
219 dominated by sea salt (NaCl).



220 By restricting our focus to segments of the CCOPE data associated with sea surface
221 trajectories (Sect. 3.1), we will analyze UHSAS-derived concentrations of particles with $D > 0.5$
222 μm ($N_{>0.5}$) and will assume that this subset of the ASD corresponds to SSA particles. This lower-
223 limit size is a factor of two smaller than the $RH = 80\%$ diameter corresponding to the middle of
224 LS04's small SSA class. This is because we assumed that particle size decreased as the aerosol
225 stream warmed from its ambient temperature to the temperature of the UHSAS measurement.
226 Support for this assumption is provided in Appendix A.

227 3.3 Moments of the Aerosol Size Distribution

228 In our analysis, we calculated three moments of the UHSAS-measured ASDs. These are
229 the aerosol concentration (N_{UHSAS}), aerosol surface area (S_{UHSAS}), and aerosol volume (V_{UHSAS}).
230 We symbolize these moments as integrals (Eq. (2) – (4)).

$$231 \quad N_{UHSAS} = \int (dN/d\log_{10}D) \cdot d\log_{10}D \quad (2)$$

$$232 \quad S_{UHSAS} = \pi \int D^2 (dN/d\log_{10}D) \cdot d\log_{10}D \quad (3)$$

$$233 \quad V_{UHSAS} = (\pi/6) \int D^3 (dN/d\log_{10}D) \cdot d\log_{10}D \quad (4)$$

234 In these formulae the group $(dN/d\log_{10}D) \cdot d\log_{10}D$ represents the concentration of aerosol
235 particles with diameter between $\log_{10}D$ and $\log_{10}D + d\log_{10}D$. Hence, when plotted versus the
236 logarithm of particle diameter, the area under the $dN/d\log_{10}D$ curve is proportional to the size-
237 integrated concentration. This is demonstrated in Figs. 4a – b where the size-integrated
238 concentration (N_{UHSAS}) is $\sim 300 \text{ cm}^{-3}$ in onshore-moving air (Fig. 4a), and the concentration is
239 approximately four times larger ($\sim 1100 \text{ cm}^{-3}$) in air thought to be contaminated by continental
240 sources (Fig. 4b). Also apparent is the right-tail of an Aitken mode, at $\sim 0.06 \mu\text{m}$ in Fig. 4a
241 (onshore-moving air), the absence of an Aitken mode in Fig. 4b (continental air), at least at
242 diameters detectable by the UHSAS ($D > 0.055 \mu\text{m}$; Table 1), and the presence of an



243 accumulation mode at $\sim 0.1 \mu\text{m}$ in both airmasses (Figs. 4a – b). Two aspects of these results, i.e.
244 the absence of an Aitken mode plus the dominance of an accumulation mode, in polluted coastal
245 air, is consistent with ASDs reported in Raes et al. (1997) and in Dall’Osto et al. (2009).

246 4 Results

247 4.1 Comparison of CPC Concentrations at Arauco Site and THD

248 In this section, Arauco site CPC concentrations are compared to concentrations measured
249 at NOAA’s THD observatory. At THD, concentrations were measured using a TSI 3760
250 condensation particle counter. The minimum particle diameter detected by the TSI 3760 ($D =$
251 $0.011 \mu\text{m}$; TSI 1996) is slightly larger than that in the TSI 3010 ($D = 0.010 \mu\text{m}$; Table 1). We
252 ignored this distinction.

253 The THD dataset spans the years 2002 to 2014. Because CCOPE was a wintertime field
254 study, only December, January, and February THD data are used in the comparison. There are
255 24,346 data points (hourly averaged) from THD and 5,541 classify as clean sector. In
256 comparison, there are 745 data points from the Arauco Site (hourly averaged) and 194 classify as
257 clean sector. For both sites we required a clean sector wind speed $> 1.5 \text{ m s}^{-1}$ in addition to the
258 clean sector directional criteria (Fig. 2). Because the numerical filter (Sect. 3.1) requires 1 Hz
259 CPC measurements, and since 1 Hz measurements are unavailable in the THD data archive, the
260 filter was not applied to either of the data sets analyzed in this section.

261 In the following paragraph we compare hourly averages of CPC measurements from the
262 Arauco Site and THD. Because the number of data points in these data sets is different, a
263 particular statistical comparison methodology was applied. The approach followed here
264 compares the Arauco and THD average concentrations by applying the Student’s t-distribution



265 method (t-test) explained in Havlicek and Crain (1988; their Eq. (10.6) and (10.7)). The
266 statistical hypotheses are: A) Null hypothesis: averages are equal, and B) Alternate hypothesis:
267 the averages are different. We also applied the non-parametric Wilcoxon Rank-Sum Test
268 (rs_test; Interactive Data Language, Harris Geospatial Solutions, Inc.). Statistical inference that
269 we derive based on the Wilcoxon Rank-Sum Test (not shown) is consistent with what we
270 describe below using the t-test.

271 Two aspects of the Arauco/THD comparison are presented here; more detail is available
272 in Fults (2016). First, clean sector concentrations are compared. The mean N_{CPC} at Arauco is
273 2759 cm^{-3} (standard deviation $\sigma = 1827 \text{ cm}^{-3}$). The mean and σ at THD are $858 \pm 729 \text{ cm}^{-3}$. Fig. 5
274 shows the Arauco and THD N_{CPC} probability distribution functions. Of note is the larger mode
275 concentration and broader distribution at Arauco. Based on our t-test comparison, the Arauco
276 average is larger than the THD average ($p < 0.01$). Second, Arauco and THD concentrations are
277 compared without regard to wind direction. The average at the Arauco Site is $2971 \text{ cm}^{-3} \pm 1802$
278 while at THD the average is $1059 \text{ cm}^{-3} \pm 855 \text{ cm}^{-3}$. These averages are also statistically different
279 ($p < 0.01$), and again, the Arauco average is larger than that at THD. Furthermore, based on the
280 averages presented in this section, and the information presented in Table 2, we classify THD as
281 a moderately-polluted marine site, and the Arauco Site as between moderately-polluted marine
282 and heavily-polluted marine.

283 4.2 Continental Contamination

284 In this section we probe why aerosol properties varied strongly during four of the 20
285 onshore trajectories. Among these, the example presented in Figs. 6a – c exhibits the largest
286 degree of CPC and UHSAS variability. During this two-hour data segment, centered on 00 UTC
287 June 9 (9 pm local time), winds were light at Arauco and Curanilahue ($< 2 \text{ m s}^{-1}$) and the wind



288 direction was variable at Curanilahue (Arauco Site wind direction measurements are only
289 available after 19 June 2015; Sect. 2.1).

290 Over the ocean, 12 to 6 hours prior to 00 UTC June 9, the HYSPLIT wind speed was 8.3
291 m s^{-1} and the HYSPLIT direction was westerly (Fig. 3b). In terms of UHSAS measurements
292 (Figs. 6a – c), an obvious feature is the variability in the sequences of N_{UHSAS} , V_{UHSAS} , and S_{UHSAS} .
293 The S_{UHSAS} is largest during an enhancement at $\sim 00:37$ UTC. The question arises: Can winds
294 over the ocean and the resultant SSA production cause this variability, or must continental
295 aerosol sources be evoked to explain this? This was addressed by calculating aerosol surface
296 areas as a function of wind speeds that bracket the HYSPLIT-derived wind speed (8.3 m s^{-1}). The
297 basis for this calculation is the *S-on-U* parameterization described in LS04 (their Fig. 22). The
298 calculation indicates that *S* can range between $6 \mu\text{m}^2 \text{ cm}^{-3}$ ($U = 6.3 \text{ m s}^{-1}$) and $15 \mu\text{m}^2 \text{ cm}^{-3}$ ($U =$
299 10.3 m s^{-1}). Since the upper-limit of the predicted variation is small compared to S_{UHSAS} at \sim
300 $00:37$ UTC (Fig. 6c), and at other times in Fig. 6c, and because the wind speed variation applied
301 in the calculation is an order of magnitude larger than the variation in the HYSPLIT-derived
302 wind speed ($\pm 0.1 \text{ m s}^{-1}$), it is concluded that the aerosol enhancements seen in Figs. 6a – c are
303 not due to a wind speed increase over the ocean. Rather, we surmise that aerosols emitted by
304 continental Chilean sources were sampled during portions of the segment in Fig. 6. Vertical
305 dashed lines indicate the subset of the two-hour segment we picked (subjectively) as being
306 representative of onshore-moving air that was not affected, or only moderately affected, by
307 emissions from continental Chilean sources. However, we do not expect our conditional
308 sampling (based on HYSPLIT) and subjective picking (e.g., Fig. 6) to select aerosol properties
309 representative of pristine marine air. Rather, we view these strategies as way to isolate aerosol



310 properties associated with onshore-moving air that was less affected by continental sources
311 compared to the other portions of the CCOPE data set.

312 Portions of three other two-hour segments were also discriminated into a period of
313 onshore-moving air that was less affected by continental aerosols compared to an adjacent
314 portion (or portions) of the two-hour data segment. This is shown in the Supplementary Material.
315 Only measurements seen plotted between the vertical dashed lines in the Supplementary Material
316 are analyzed in Sect. 4.3, 4.4, and 4.5.

317 **4.3 Using N/V ratios to Parameterize Cloud Droplet Concentrations**

318 In this section we analyze the ASD moments defined by Eq. (2) and (4). These are
319 symbolized N_{UHSAS} and V_{UHSAS} , respectively. The ratio of N_{UHSAS} (aerosol concentration) and
320 V_{UHSAS} (aerosol volume) – generically the N/V ratio - is of interest for several reasons. First,
321 models that evaluate exchange between a marine boundary layer (MBL) and an overlying free
322 troposphere (FT) successfully predict the N/V ratio in the MBL (van Dingenen et al., 2000;
323 hereafter VD00). Second, a value of the ratio can be derived by fitting measurements of N and V
324 (Hegg and Kaufman 1998, hereafter HK98). Third, aerosol mass loading, and thus an aerosol
325 volume corresponding to an assumed particle density³, are relatively easy to evaluate. A method
326 routinely used to evaluate aerosol mass involves pulling aerosol-laden air through a filter and
327 evaluating the accumulated mass gravimetrically. Fourth, the product of an N/V ratio and an
328 ambient aerosol volume has been proposed for estimating cloud droplet concentrations in marine
329 stratocumulus clouds (HK98 and VD00).

³ In the case of ambient particles containing hygroscopic materials, density values range between 1.5 and 1.8 g cm⁻³ (McMurry et al. 2002)



330 HK98 used a passive cavity aerosol spectrometer probe (PCASP) to evaluate N , V and the
331 N/V ratio. Since the UHSAS counts down to a smaller diameter ($0.055\ \mu\text{m}$) than the PCASP
332 ($0.12\ \mu\text{m}$), it is expected that the N/V ratios we derive using the UHSAS will be larger than those
333 in HK98. The main reason for this is that decreasing the lower-limit diameter increases N more
334 than V (VD00).

335 As in HK98, linear least-squares regression analysis with an equation of the form $Y = a \cdot X$
336 was used to derive N/V ratios. Values of N_{UHSAS} and V_{UHSAS} entered into the regressions were
337 derived with the lower-limit diameter set at $0.055\ \mu\text{m}$ (Table 3) and $0.12\ \mu\text{m}$ (Table 4). The latter
338 allows comparison to N/V ratios in HK98. Tables 3 and 4 show the ratios and the fact that all of
339 the Pearson correlation coefficients (r) are positive. With the exception of trajectories arriving at
340 12 UTC June 5 and 06 UTC June 8 (Table 3), and at 00 UTC June 9 (Table 4), all of the N/V
341 correlations are statistically significant at $p < 0.01$.

342 As expected, the average N/V ratio in the fifth column of Table 3 ($417 \pm 297\ \mu\text{m}^{-3}$) is
343 larger than that in HK98 ($223 \pm 76\ \mu\text{m}^{-3}$). These averages are different at $p = 0.01$. Table 4 has
344 results based on the larger lower-limit diameter ($0.12\ \mu\text{m}$). In that comparison, the Arauco N/V
345 ratio ($159 \pm 100\ \mu\text{m}^{-3}$) does not differ significantly from HK98's (i.e., $p > 0.01$).

346 Application of the N/V ratio to aerosol-cloud-precipitation modelling requires knowledge
347 of the aerosol volume, or alternatively, knowledge of the aerosol mass loading and the aerosol
348 particle density. The aerosol volume is then multiplied by an average N/V ratio (e.g., the average
349 at the bottom of the fifth column of Table 4), and their product is taken to be the modelled cloud
350 droplet concentration (HK98 and VD00). This is straight forward, at least from the perspective of
351 incorporating an aerosol-induced cloud feedback into a simulation, but it suffers from requiring
352 additional information about the aerosol (aerosol volume). Because the UHSAS was unavailable



353 for much of CCOPE (Table 1), aerosol volume is also unavailable. Another drawback is the
354 implicit assumption that only aerosol particles larger than the lower-limit diameter (e.g., 0.12 μm
355 in Table 4) form cloud droplets.

356 4.4 Using ASD and N_{CPC} Measurements to Parameterize CCN Activation Spectra

357 Andreae (2009) analyzed a set of aerosol concentration measurements obtained from
358 collocated CPC and CCN instruments. Andreae's CPC measurements represent the concentration
359 of particles *no smaller than* a particular diameter ($\sim 0.01 \mu\text{m}$; Table 1), and his CCN
360 measurements represent the concentration of particles that activate cloud droplets at a water
361 vapor supersaturation (SS) *no larger than* a particular value (Rogers and Yau, 1989; chapter 6).
362 The latter is $SS = 0.4 \%$ in Andreae (2009).

363 Similar to the relationship between CCN concentrations at $SS = 0.4 \%$ and CPC
364 concentrations (Andreae, 2009; his Fig. 2), we now describe how CPC and UHSAS
365 concentrations from CCOPE can be used to develop functions that describe CCN activation
366 spectra. In our development, the independent variable is a CPC-measured aerosol concentration.
367 While only estimates, the activation spectra we obtain represent an important step toward
368 evaluating how CCN affected cloud and precipitation during CCOPE. We envision that this
369 assessment will be advanced when our activation spectra are used to initialize numerical models.

370 Our first step is to select a particle diameter, apply this as a lower-limit diameter in Eq.
371 (2), and divide the resultant size-integrated UHSAS concentration by the coincident CPC-
372 measured concentration. Two examples of this are presented in Figs. 7a – b where we define the
373 UHSAS-to-CPC concentration ratio as a *fractional aerosol concentration (FAC)*. We symbolize
374 these as $FAC(D=0.055 \mu\text{m})$ (Fig. 7a) and as $FAC(D=0.120 \mu\text{m})$ (Fig. 7b). As is illustrated, a



375 *FAC* can be interpreted as the fraction of the aerosol population *no smaller than* the lower-limit
376 diameter at the left-edge of the gray shading.

377 In a second step we interpret a *FAC*'s lower-limit diameter as an upper-limit *SS*. We do
378 this by applying a value for the kappa hygroscopicity parameter, which we set at $\kappa = 0.5$, and by
379 applying the kappa–Köhler formula of Petters and Kreidenweis (2007, their Eq. (11)). This
380 transformation from lower-limit *D* to upper-limit *SS* converts the *FAC* in Fig. 7a to *FAC*(*SS* =
381 0.41 %) and the *FAC* in Fig. 7b to *FAC*(*SS* = 0.13 %). We also evaluated how a range of the
382 kappa parameter ($0.3 < \kappa < 0.7$) translates to a range of *SS*. Our upper-limit κ comes from
383 airborne measurements made over the Southeast Pacific Ocean during summer (Snider et al.,
384 2017), and our lower-limit κ is the value recommended by Andreae and Rosenfeld (2008) for
385 simulating aerosol indirect effects over continents.

386 The *FAC*s in Figs. 7a – b are two examples of the many available from CCOPE. We
387 derived averaged *FAC*s, corresponding to each of five $N_{UHSAS}(D)$ sets (corresponding to five
388 selected lower-limit diameters ($D = 0.055, 0.070, 0.095, 0.120, \text{ and } 0.200 \mu\text{m}$)), by plotting
389 $N_{UHSAS}(D)$ versus N_{CPC} and fitting the data with the equation $Y = a \cdot X$ where $Y = N_{UHSAS}(D)$, $X =$
390 N_{CPC} , and “*a*” is the averaged *FAC*.

391 Averaged *FAC*s are presented in the seventh columns of Tables 3 and 4 where we
392 symbolize these as *FAC*($D = 0.055 \mu\text{m}$) and *FAC*($D = 0.120 \mu\text{m}$), respectively. Correlation
393 coefficients presented in the eighth columns of these tables mostly exceed 0.5. By averaging over
394 each of the 20 onshore trajectories, and noting that four of these were limited to a time interval
395 shorter than the nominal two hours (Sect. 4.2 and Tables 3 and 4), we calculated the overall
396 averages presented at the bottom of the two tables. These overall averages are *FAC*($D = 0.055$
397 μm) = 0.35 ± 0.13 (Table 3) and *FAC*($D = 0.120 \mu\text{m}$) = 0.13 ± 0.07 (Table 4). This decrease of



398 the *FAC* results because a larger lower-limit D (Eq. (2)), implies a smaller $N_{UHSAS}(D)$, and thus a
399 smaller $FAC(D)$.

400 What we refer to as *ensemble-averaged FACs* were calculated by combining N_{CPC} and
401 $N_{UHSAS}(D)$ values from all of the onshore trajectories. The selected data pairs were fitted in the
402 manner discussed previously. In addition, upper and lower quartile values of the fitted slopes
403 were calculated by applying the technique of Wolfe and Snider (2012; their Fig. 4d). We
404 evaluated four ensemble-averaged *FACs* corresponding to four selected diameters ($D = 0.070$,
405 0.095 , 0.120 , and $0.200 \mu\text{m}$). The *FAC* at $D = 0.055 \mu\text{m}$ was eliminated from this analysis
406 because Kupc et al. (2018) showed that UHSAS-measured concentrations, at $D \leq 0.070 \mu\text{m}$, are
407 negatively biased. Results are presented as circles in Fig. 8 and vertical error bars represent the
408 quartile range. Values plotted on the abscissa correspond to the four diameters, each transformed
409 to an SS using the kappa–Köhler formula with $\kappa = 0.5$, and horizontal error bars extend from
410 most hygroscopic ($\kappa = 0.7$), at the left-most limit, to least hygroscopic ($\kappa = 0.3$), at the right-most
411 limit.

412 In Fig. 8 we used power laws of the form $FAC(SS) = C \cdot SS^k$ (i.e., the form commonly used
413 to parameterize CCN activation spectra (Twomey 1959)) to fit the points. The change in the
414 slope of the fit function, seen here at $SS = 0.15\%$, seems consistent with analyses demonstrating
415 that in polluted marine cloud conditions, albeit during summertime, the exponent “ k ” in the
416 Twomey power fit function is ≥ 1 and ≤ 1 at $SS < 0.1\%$ and $SS > 0.1\%$, respectively (Hudson
417 and Nobel 2014; data from the MASE project in their Fig. 1).

418 Our parameterized CCN activation spectrum (Fig. 8) is relevant to cloud-aerosol-
419 precipitation modeling for several reasons. First, some numerical models treat SS as a prognostic
420 variable and thus require initialization with a CCN activation spectrum (e.g., Khairoutdinov and



421 Kogan 2000). Similarly, some models initialize with a particle size-dependent ASD function and
422 use Köhler theory to derive a model-initializing CCN activation spectrum (e.g., Lebo et al.
423 2012). As described in these two references, these models initialize with a nonspecific CCN
424 activation spectrum. If those models were used to investigate wintertime clouds and precipitation
425 on the Central Chilean Coast, our parameterization could be applied as a CCOPE-specific
426 initialization. Second, since we have measurements of N_{CPC} for the totality of CCOPE (Table 1),
427 and we have shown how an ensemble-averaged CCN activation spectrum can be developed with
428 N_{CPC} as the input parameter – i.e. as $N(SS) = FAC(SS) \cdot N_{CPC}$ – our parameterization can be used
429 to estimate activation spectra for the complete CCOPE campaign. Third, model initiation with a
430 specific CCN activation spectrum, as opposed to initialization with a regime-dependent droplet
431 concentration (e.g., Thompson et al. 2004), is justified by sensitivities to cloud droplet activation
432 reported in several publications (Cooper et al. 1997; Hudson and Yum, 1997; Snider et al.,
433 2017).

434 An assumption implicit in our development is that particles were internally mixed within
435 each of the four particle size classes. This seems justified by our use of HYSPLIT to
436 conditionally sample (Sect. 3.1), and by the fact that the sampled airmasses were resident in the
437 marine boundary layer for hours to days while subject to a variety of processes (Brownian
438 coagulation and reactive uptake of SO_2 , among others) that produce aerosols consistent with the
439 internal mixture assumption (Fierce et al. 2017). An aspect of the measurements also supports
440 the internal mixture assumption. Fig. 7b shows that number concentration corresponding to the
441 0.120 to 1 μm class is dominated by particles with diameters at the lower end of that class.
442 Hence, the contribution of freshly emitted SSA particles, generally thought to size at dry
443 diameters larger than 0.5 μm (Clarke et al. 2003; LS04), and with a $\kappa = 1.2$ (Berg et al. 1998), is



444 typically small. A different bias would result if particles with κ values smaller than the lower-
445 limit value ($\kappa = 0.3$) contributed significantly to an $N_{UHSAS}(D)$ class. Burning biomass is an
446 important source for such low-hygroscopicity particles (Carrico et al. 2005). Our conditional
447 sampling (Sect. 3.1), combined with our filtering of the CPC and UHSAS measurements (Sect.
448 3.1 and Appendix B), reduces this concern.

449 4.5 Regression of $N_{>0.5}$ and Sea Surface Wind Speed

450 As discussed in Sect. 3.2, $N_{>0.5}$ represents the concentration of particles larger than 0.5
451 μm . We now support our conjecture that particles grouped into the $N_{>0.5}$ subset are indeed SSA.
452 We do this by analyzing the correlation between $N_{>0.5}$ and sea surface wind speed (U). Sect. 3.1
453 explains how we used HYSPLIT to derive U .

454 Values of $N_{>0.5}$, corresponding to the 18 sea surface trajectories (Sect. 3.1), are plotted
455 against U in Fig. 9. Linear least-squares regression analysis with a model equation of form
456 $\ln(N_{>0.5}) = \ln(N_o) + a_N \cdot U$ was used to derive the coefficients N_o and a_N (O'Dowd and Smith
457 1993; LS04). The fitted coefficients are $N_o = 0.15 \text{ cm}^{-3}$ and $a_N = 0.38$ and the derived function
458 (black curve) is shown in Fig. 9. The dashed black curves represent the 95% confidence interval
459 (Romano 1977; his Eq. (4.2.3.f)). Also plotted (pink line) is the function derived by O'Dowd and
460 Smith (1993) during ship-based sampling for dried particles with diameter between 0.38 and
461 0.84 μm . Given that the O'Dowd and Smith (1993) function (their Fig. 7a) is associated with
462 statistical uncertainty comparable to what we estimate for our data set, we are only moderately
463 confident that the function we derived is a consequence of wind-generated SSA. Two caveats
464 require mentioning. First, a fraction of our data points ($\sim 25\%$) lie either above or below our
465 confidence interval (Fig. 9). Meteorology can contribute to this variability, as when sea surface
466 winds establish a SSA population, and the wind subsequently slacks, or speeds up, prior to



467 advection onto the continent. This is expected because the atmospheric residence time of $D \sim 0.5$
468 μm particles, in the absence of precipitation, is several days (LS04, p. 76). Also, our
469 unintentional sampling of particles generated over the continent is a concern. We have taken
470 steps to eliminate those sources of contamination (Sect. 3.1 and Appendix B), but our methods
471 are not foolproof.

472 5 Discussion

473 The measurements analyzed here are, to the best of our knowledge, the first to
474 characterize aerosol concentrations and aerosol size distributions on the Central Chilean Pacific
475 coast during winter. Since the measurement site was relatively close to a population center
476 (Arauco, Chile), and a SO_2 emitting paper mill, and because wood burning is an important source
477 of residential heat in this region, we suspect that our measurements are influenced by these land
478 sources. We mitigated against this by focusing on data collected during periods of onshore flow.
479 Additional steps were taken to minimize contamination from land-based aerosol sources. These
480 procedures are explained in Sect. 3.1, 4.2, Appendix B, and in the Supplementary Material.

481 A point of comparison is the summertime measurements reported in HK98. Their data
482 was collected during airborne sampling over the western Atlantic in air that had advected from
483 the United States. HK98's averaged aerosol surface area ($131 \pm 93 \mu\text{m}^2 \text{cm}^{-3}$; their Table 2) is
484 clearly larger than that for our 20 onshore trajectories ($42 \pm 27 \mu\text{m}^2 \text{cm}^{-3}$; results not shown).
485 However, a more relevant comparator would be low altitude measurements made off the Central
486 Chilean Pacific during winter. As far as we know, the desired data set is not available. Values of
487 aerosol surface area in the FT over the North and South Pacific are generally $< 10 \mu\text{m}^2 \text{cm}^{-3}$
488 (Clarke 1992), suggesting that even during onshore flow the Arauco Site measurements are



489 affected by anthropogenic sources. We have assumed these sources are Chilean, however, a
490 contribution from long range transport cannot be ruled out.

491 The larger wintertime-averaged CPC concentration at Arauco, compared to THD, is
492 evidence for stronger continental contamination at Arauco. Since N_{CPC} is a parameter in our
493 parameterization of CCN activation spectra (Sect. 4.4), we conclude that cloud droplet
494 concentrations in low level marine clouds (stratocumulus) formed in the vicinity of Arauco are
495 larger than in similar clouds near THD. If true, this conclusion would be opposite the general
496 situation in Southern Pacific boundary layer clouds where cloud droplet concentrations are
497 statistically less than in their Northern hemispheric counterparts (Bennartz 2007). Relevant to
498 this, Bennartz (2007) comments on a coast-normal droplet concentration gradient that is stronger
499 on the Central Chilean coast compared to the California/Oregon coast. We presume that the
500 gradient exists because of the larger concentration of aerosols over continents (Andreae and
501 Rosenfeld, 2008), and because of aerosol removal that occurs within and below marine
502 stratocumulus clouds. In addition, Bennartz (2007) demonstrates that the coast-normal droplet
503 concentration gradient is larger off the Central Chilean coast, compared to California/Oregon
504 coast, in part because oceanic concentrations, ~ 2000 km offshore, are generally smaller in the
505 south compared to the north Pacific. Whether the southern hemispheric gradient is also enhanced
506 by larger aerosol concentrations over coastal Central Chile, compared to coastal California and
507 Oregon, is an open question. Further analysis of the satellite retrievals analyzed by Bennartz
508 (2007), with segregation into wintertime and summertime categories, as well as measurements
509 conducted at an offshore island location, or acquired using aircraft or ships, are needed to resolve
510 this question.

511



512 6 Conclusions

513 Analyses presented here are based on Condensation Particle Counter (CPC)
514 measurements made during one winter season (June, July and August 2015) on the Central
515 Chilean Pacific coast (38 ° S). Also analyzed are aerosol size distribution measurements made
516 with an Ultra High Sensitivity Aerosol Spectrometer (UHSAS). UHSAS measurements are
517 available from 29 May to 28 June (Table 1). Limitations of this study are proximity of the
518 measurement site to a population center (Arauco, Chile) and a SO₂ emitting paper mill, sampling
519 of particles emitted from residences close to where our instruments were operated, and the
520 incomplete drying of the sampled aerosol particles. This first attempt to make CPC and ASD
521 measurements on the Central Chilean Pacific coast during winter was exploratory and our results
522 should be considered preliminary.

523 We compared the Arauco Site CPC measurements to values acquired at the NOAA
524 observatory Trinidad Head (THD) on the North Pacific Coast of California. Averaged CPC
525 concentrations are larger at the Arauco Site and that difference is evident in Arauco/THD
526 comparisons based on air arriving from all wind directions and from clean sector directions. In
527 addition, we conditionally sampled the UHSAS measurements and derived parameterized
528 descriptions of sea salt aerosol (SSA) and cloud condensation nuclei (CCN) for periods of
529 onshore flow. In these parameterizations the input parameters are respectively sea surface wind
530 speed and CPC-measured aerosol concentration.

531 In the context of CCOPE, there are two precipitation regimes that impact the Central
532 Chilean Coast and the Nahuelbuta Mountains during winter (Massmann et al. 2017). The first of
533 these have radar-derived echo tops at ~ 2 km MSL and produce rain by direct conversion of
534 cloud droplets to rain drops. The second have higher echo tops, extending to temperatures colder



535 than 0 °C and produce rain that is, at least in part, initiated by ice phase processes. Investigation
536 of the rain produced in the shallow regimes is an active area research; it is thought that SSA and
537 the CCN play important roles (Feingold et al. 1999; Gerber and Frick 2012). The deep regimes
538 form precipitating hydrometeors (ice particles) at cloud temperatures < 0 °C. Again, aerosols
539 play a role, but there are many facets to this and first-order effects are not yet agreed on. Perhaps
540 foremost is the role played by aerosol acting as ice nuclei. Measurement of an ice nuclei
541 activation spectrum, development of an ice particle parameterization, and incorporation of the
542 parameterization into a numerical model are needed to explore this dimension of the problem.
543 Because they modulate cloud droplet size, the development of graupel, and influence latent
544 heating (e.g., Tao et al. 2012), the CCN and SSA likely also play a role in the deep regimes.
545 Thus, we anticipate that modeling of both precipitation regimes will benefit from the CCN and
546 SSA parameterizations presented here.



547 **Author Contribution**

548 Jeff Snider, Jason Minder, David Kingsmill wrote successful proposals that funded this
549 research. Sara Fults, Adam Massman, Aldo Montecinos, and David Kingsmill performed the
550 field measurements. René Garreaud and Aldo Montecinos provided logistical support during the
551 field phase of the project. Elisabeth Andrews provided data from THD. Sara Fult wrote her MS
552 dissertation and this was adapted to this manuscript by Jeff Snider. All authors contributed to the
553 editing of this manuscript.

554 **Acknowledgments**

555 We thank Freddy Echeverría-Cabezas for his assistance during CCOPE, Matthew
556 Burkhart for building the aerosol data acquisition system, Zhien Wang for providing a graduate
557 assistantship, Nicholas Mahon for shipping logistics, and the Departamento de Geofísica at the
558 Universidad de Concepción. This work was supported by the United States National Science
559 Foundation Physical and Dynamic Meteorology Division under Awards AGS-1522277 and
560 AGS-1522939.

561 **Data Availability**

562 CCOPE CPC and UHSAS data, and a data reader (Interactive Data Language, Harris
563 Geospatial Solutions, Inc.), are at <http://www-das.uwyo.edu/~jsnider/CCOPE/>.

564

565 **Appendix A:**

566 Because the RH at the Arauco Site was often in excess of 80 % (Fig. A1c), particles
567 entering the sample tube (Sect. 2.2) were haze droplets (Rogers and Yau 1989). As these haze
568 droplets transit the sample tube they experience an increase in temperature, an RH decrease, and
569 thus a decreased D . The lowest RH experienced by a haze droplet is at the point of detection
570 where the aerosol temperature is presumed to be the internal “box temperature” measured by the
571 UHSAS. The RH at this point is

$$572 \quad RH_U = \frac{RH_A \cdot e_s(T_A)}{e_s(T_U)} \quad (A1)$$

573 where T_U is the internal UHSAS temperature, e_s is saturation vapor pressure (temperature
574 dependent), and RH_A and T_A are the ambient RH and temperature, respectively. In nearly all of
575 the UHSAS sampling during CCOPE, the RH_U was less than 60 % (Fig. A1d). This suggests that
576 the haze droplets detected by the UHSAS were partially dried. Partial drying of the haze droplets
577 is supported by thermodynamic calculations (Lewis and Schwartz 2004; their Fig. 8) showing
578 that a $D = 4 \mu\text{m}$ NaCl haze droplet reaches its equilibrium size ($D = 2 \mu\text{m}$) in 0.1 s subsequent to
579 a step-change of RH from 98 % to 80 %. Because 0.1 s is small relative to the average residence
580 time of haze droplets within the sample tube (0.8 s), we ignored the possibility of a kinetic
581 limitation to drying and we assumed that the haze droplets relaxed to their equilibrium size at
582 RH_U prior to the time they were detected. Since we do not know the chemical composition of the
583 haze droplets, their equilibrium size is not specifiable, but calculations corresponding to $RH_U =$
584 60% and a haze droplet composed of sodium sulfate indicate that the equilibrium size is 30%
585 larger than the corresponding dry particle size (Snider et al. 2017; their Fig. A2b). Three factors
586 interact to partially compensate for a size overestimate due to incomplete particle drying during



587 CCOPE: 1) Particle sizing performed by the UHSAS was calibrated using polystyrene latex
588 particles (refractive index $n = 1.57$ at $\lambda = 1.05 \mu\text{m}$ (Marx and Mulholland 1983)); 2) Liquid water
589 ($n = 1.32$ at $\lambda = 1.05 \mu\text{m}$ (Irvine and Pollack, 1968)) makes a significant contribution to the mass
590 of a haze droplet at $RH = 60\%$ (here again we are assuming the above-mentioned sodium sulfate
591 composition for the completely dried particle); and 3) Assuming the same scattering intensity, an
592 $n = 1.6$ particle sizes 10% smaller than an $n = 1.4$ particle (Cai et al., 2008; their Fig. 1).
593 Accepting the 10% as an underestimate, and the above-mentioned 30% as an overestimate, we
594 conclude that particle sizes reported by the UHSAS were overestimated by 20%. We did not
595 correct for this sizing bias.

596 Laboratory testing of the UHSAS and CPC is documented in Figs. A2a – b, and in Figs.
597 A3a - b. We evaluated consistency among measurements made with the UHSAS, the CPC, and a
598 Scanning Mobility Particle Scanner (SMPS; TSI 2000b). In all of these tests, the RH of the test
599 aerosols was $< 15\%$. An example ASD derived using the UHSAS (pink) and the SMPS (black)
600 is shown in Fig. A2a. In this test the three instruments (UHSAS, CPC and SMPS) were sampling
601 mobility-selected ammonium sulfate particles with $D = 0.075 \mu\text{m}$. The refractive index of this
602 material at $\lambda = 1.05 \mu\text{m}$ is $n = 1.51$ (Toon et al., 1976). It is evident that the mode diameter
603 measured by the UHSAS is smaller than that reported by the SMPS ($D = 0.075 \mu\text{m}$). This
604 difference is qualitatively consistent with the smaller refractive index of the test material
605 (ammonium sulfate), compared to the larger refractive index of the polystyrene latex particles
606 used by the factory to calibrate the UHSAS (DMT, 2013). Fig. A2b shows a test with $D = 0.71$
607 μm polystyrene latex particles. As expected, the mode diameter in the UHSAS size distribution
608 is in agreement with the mode size in the SMPS size distribution.



609 An additional feature of our laboratory testing is the multi-modal structure in the SMPS
610 size distribution at $D < 0.5 \mu\text{m}$ (Fig A2b). This structure results because the particle diameter
611 inferred by the SMPS depends on the physical diameter of the test particles, and on also depends
612 on the test particle's charge state. The multi-modal structure at $D < 0.5 \mu\text{m}$ corresponds to
613 particles carrying 5, 4, 3, and 2 fundamental charges, but each with physical diameter equal 0.71
614 μm . As stated in the previous paragraph, the latter is the diameter of the polystyrene test
615 particles.

616 Figs. A3a - b summarize all of the lab testing we conducted in support of CCOPE. In Fig.
617 A3a, N_{UHSAS} is plotted vs N_{CPC} for tests with $D < 0.2 \mu\text{m}$ and Fig. A3b has tests with $D > 0.2 \mu\text{m}$.
618 On average, concentrations differ by $\pm 6 \%$ in Fig. A3a ($D < 0.2 \mu\text{m}$) and by $\pm 10 \%$ in Fig. A3b
619 ($D > 0.2 \mu\text{m}$).

620



621 **Appendix B:**

622 For each of the onshore trajectories (Sect. 3.1), a two-hour segment, centered on the
623 trajectory arrival time was analyzed. An example is in Figs. B1a – e. Fig. B1a shows the
624 sequence of CPC values sampled every second (i.e., 1-s samples referred to as *fast* N_{CPC}), and
625 Fig. B1b shows CPC values sampled every 10 seconds (i.e., 10-s samples referred to as *slow*
626 N_{CPC}). The following procedure was used to attenuate the narrow perturbations (e.g., within the
627 time interval indicated by vertical dashed lines in Figs. B1a, B1b, and B1d) that were likely the
628 result of local aerosol emissions.

629 First, the fast N_{CPC} values were used to determine, for each 10 s of the sequence, a
630 concentration relative standard deviation ($\sigma / \langle x \rangle$). Second, if the relative standard deviation was
631 greater than 0.02 both the slow N_{CPC} measurement (sampled once every 10 second) and the ASD
632 measurement (also sampled once every 10 second; Table 1) were discarded. Fig. B1c and Fig.
633 B1e show the N_{CPC} and N_{UHSAS} sequences after application of the filter. These two filtered
634 sequences ($N_{CPC}(\text{filtered})$ and $N_{UHSAS}(\text{filtered})$), and the filtered values of aerosol surface area
635 (S_{UHSAS}), aerosol volume (V_{UHSAS}), and $D > 0.5 \mu\text{m}$ concentration ($N_{>0.5}$) are the focus of the bulk
636 of our analysis.

637

638 **References**

- 639 Albrecht, B. A., Aerosols, cloud microphysics, and fractional cloudiness, *Science*, 245, 1227 –
640 1230, 1989
641
- 642 Andreae, M.O., Correlation between cloud condensation nuclei concentration and aerosol optical
643 thickness in remote and polluted regions, *Atmos. Chem. Phys.*, 9, 543-556, 2009
644
- 645 Andreae, M.O. and D. Rosenfeld, Aerosol-cloud-precipitation interactions. Part 1. The nature
646 and sources of cloud-active aerosols, *Earth-Sci. Rev.*, 89, 13 – 41, 2008
647
- 648 Arauco Woodpulp, accessed 16 December 2018 at:
649 http://web.arauco.cl/_file/file_3382_pulp%20catalog.pdf, 2010
650
- 651 Bennartz, R., Global assessment of marine boundary layer cloud droplet number concentration
652 from satellite, *J. Geophys. Res.*, 112, D02201, 2007
653
- 654 Berg, O. H., E. Swietlicki, and R. Krejci, Hygroscopic growth of aerosol particles in the marine
655 boundary layer over the Pacific and Southern Oceans during the First Aerosol
656 Characterization Experiment (ACE 1), *J. Geophys. Res.*, 103, 16535-16545, 1998
657
- 658 Birmili, W., A. Wiedensohler, J. Heintzenberg, and K. Lehmann, Atmospheric particle number
659 size distribution in central Europe: Statistical relations to air masses and meteorology, *J.*
660 *Geophys. Res. Atmos.*, 106, 32005–32018, 2001
661
- 662 Boucher, O., and Coauthors, Clouds and Aerosols. In: *Climate Change 2013: The Physical*
663 *Science Basis. Contribution of Working Group I to the Fifth Assessment Report of the*
664 *Intergovernmental Panel on Climate Change* [Stocker, T.F., D. Qin, G.-K. Plattner, M.
665 Tignor, S.K. Allen, J. Boschung, A. Nauels, Y. Xia, V. Bex and P.M. Midgley (eds.)],
666 Cambridge University Press, Cambridge, United Kingdom, 2013
667
- 668 Brechtel, F. J., S. M. Kreidenweis, and H. B. Swan, Air mass characteristics, aerosol particle
669 number concentrations, and number size distributions at Macquarie Island during the
670 First Aerosol Characterization Experiment (ACE 1), *J. Geophys. Res. Atmos.*, 103,
671 16351–16367, 1998
672
- 673 Cai, Y., J.R. Snider and P. Wechsler, Calibration of the passive cavity aerosol spectrometer
674 probe for airborne determination of the size distribution, *Atmos. Meas. Tech.*, 6, 2349-
675 2358, 2013
676
- 677 Cai, Y., D.C. Montague, W. Mooiweer-Bryan and T. Deshler, Performance characteristics of the
678 ultra high sensitivity aerosol spectrometer for particles between 55 and 800 nm:
679 Laboratory and field Studies, *J. Aerosol Sci.*, 39, 759-769, 2008
680



- 681 Carrico, C.M., S.M.Kreidenweis, W.C.Malm, D.E.Day, T.Lee, J.Carrillo, G.R.McMeeking, J.L.
682 Collett, Hygroscopic growth behavior of a carbon-dominated aerosol in Yosemite
683 National Park, Atmos. Environ., 39, 1393-1404, 2005
684
- 685 Clarke, A., Atmospheric Nuclei in the Remote Free-Troposphere, J. Atmos. Chem., 14, 479-488,
686 1992
- 687 Clarke, A., V. Kapustin, S. Howell, K. Moore, B. Lienert, S. Masonis, T. Anderson, and D.
688 Covert, Sea-salt size distribution from breaking waves: Implications for marine aerosol
689 production and optical extinction measurements during SEAS, J. Atmos. Ocean.
690 Technol., 20, 1362–1374, 2003
691
- 692 Cooper, W.A., R.T. Bruintjes, and G.K. Mather, Calculations pertaining to hygroscopic seeding
693 with flares, J. Appl. Meteor., 36, 1449 – 1469, 1997
694
- 695 Covert, D. S., V. N. Kapustin, P. K. Quinn, and T. S. Bates, New particle formation in the
696 marine boundary layer, J. Geophys. Res., 97(D18), 20581–20589,
697 doi:10.1029/92JD02074, 1992
698
- 699 Dall’Osto, M., and Coauthors, Aerosol properties associated with air masses arriving into the
700 North East Atlantic during the 2008 Mace Head EUCAARI intensive observing period:
701 an overview, Atmos. Chem. Phys. Discuss., 9, 26265–26328, 2009
702
- 703 Diesch, J. M., F. Drewnick, S. R. Zorn, S. L. Von Der Weiden-Reinmüller, M. Martinez, and S.
704 Borrmann, Variability of aerosol, gaseous pollutants and meteorological characteristics
705 associated with changes in air mass origin at the SW Atlantic coast of Iberia, Atmos.
706 Chem. Phys, 12, 3761-3782, 2012
707
- 708 DMT, Ultra High Sensitivity Aerosol Spectrometer (UHSAS) Operator Manual, Boulder, CO,
709 2013
710
- 711 Feingold, G., W. R. Cotton, S. M. Kreidenweis, J. T. Davis, and J. A. T. D. Avis, The Impact of
712 Giant Cloud Condensation Nuclei on Drizzle Formation in Stratocumulus: Implications
713 for Cloud Radiative Properties, J. Atmos. Sci., 56, 4100–4117, 1999
714
- 715 Fierce, L., N. Riemer, and T.C. Bond, Toward Reduced Representation of Mixing State for
716 Simulating Aerosol Effects on Climate. Bull. Amer. Meteor. Soc., 98, 971–980,
717 <https://doi.org/10.1175/BAMS-D-16-0028.1>, 2017
718
- 719 Fults, S., Aerosol measurements during the Central Chilean Orographic Precipitation
720 Experiment, M.S. Thesis, Department of Atmospheric Science, University of Wyoming,
721 2016
722
- 723 Garreaud, R., M.Falvey, and A.Montecinos, Orographic precipitation in coastal southern Chile:
724 Mean distribution, temporal variability, and linear contribution, J. Hydrometeor., 1185 –
725 1202, 2016
726



- 727 Gerber, H. and G.Frick, Drizzle rates and large sea-salt nuclei in small cumulus, *J. Geophys.*
728 *Res.*, 117, D01205, 2012
729
- 730 Gras, J.L., Baseline atmospheric condensation nuclei at Cape Grim 1977-1987, *J. Atmos. Chem.*,
731 11, 89-106, 1990
732
- 733 Gras, J. L., CN, CCN and particle size in Southern Ocean air at Cape Grim, *J. Atmos. Res.*,
734 35, 233–251, 1995
735
- 736 Hansen, J., *The Faustian Bargain: Humanity's Own Trap, Storms of My Grandchildren*,
737 Bloomsbury, 320 pp., 2009
738
- 739 Havlicek, L.L., and R.D. Crain, *Practical Statistics for the Physical Sciences*, American
740 Chemical Society, 512 pp., 1988
741
- 742 Hegg, D. A., and Y. J. Kaufman, Measurements of the relationship between submicron aerosol
743 number and volume concentration, *J. Geophys. Res.*, 103, 5671-5678, 1998
744
- 745 Hinds, W. C., *Aerosol Technology: Properties, Behavior and Measurement of Airborne*
746 *Particles*, John Wiley & Sons, INC, 483, 1999
747
- 748 Hoppel, W. a., G. M. Frick, J. W. Fitzgerald, and R. E. Larson, Marine boundary layer
749 measurements of new particle formation and the effects nonprecipitating clouds have, *J.*
750 *Geophys. Res.*, 99, 14443–14459, 1994
751
- 752 Hudson, J.G. and S. Yum, Droplet spectral broadening in marine stratus. *J. Atmos. Sci.*, 54,
753 2642–2654, 1997
754
- 755 Hudson, J.G., and S.Nobel, CCN and vertical velocity influences on droplet concentrations and
756 supersaturations in clean and polluted stratus clouds, *J. Atmos. Sci.*, 312-331, 2014
757
- 758 Hudson, J.G., S.Noble, and S.Tabor, Cloud supersaturations from CCN spectra Hoppel minima,
759 *J. Geophys. Res. Atmos.*, 120, 3436–3452, doi:10.1002/2014JD022669, 2015
760
- 761 Irvine, W.M. and J.B. Pollack, Infrared optical properties of water and ice spheres, *Icarus*, 8, 324
762 – 360, 1968
763
- 764 Khairoutdinov, M. and Y. Kogan, A new cloud physics parameterization in a large-eddy
765 simulation model of marine stratocumulus, *Mon. Wea. Rev.*, 128, 229 - 243, 2000
766
- 767 Kupc, A., Williamson, C., Wagner, N. L., Richardson, M., and Brock, C. A.: Modification,
768 calibration, and performance of the Ultra-High Sensitivity Aerosol Spectrometer for
769 particle size distribution and volatility measurements during the Atmospheric
770 Tomography Mission (ATom) airborne campaign, *Atmos. Meas. Tech.*, 11, 369-383,
771 <https://doi.org/10.5194/amt-11-369-2018>, 2018
772



- 773 Lebo, Z. J., Morrison, H., and Seinfeld, J. H., Are simulated aerosol-induced effects on deep
774 convective clouds strongly dependent on saturation adjustment?, Atmos. Chem. Phys.,
775 12, 9941-9964, 2012
776
- 777 Lewis, E. R., and S. E. Schwartz, Sea Salt Aerosol Production: Mechanisms, Methods,
778 Measurements, and Models, American Geophysical Union, 413 pp., 2004
779
- 780 Marx, E. and G.W. Mulholland, Size and refractive index determination of single polystyrene
781 spheres, Journal of Research of the National Bureau of Standards, 88, 321 – 338, 1983
782
- 783 Massmann, A.K., J.R. Minder, R.D. Garreaud, D.E. Kingsmill, R.A. Valenzuela, A. Montecinos,
784 S.L. Fuels, and J.R. Snider, 2017, The Chilean Coastal Orographic Precipitation
785 Experiment: Observing the Influence of Microphysical Rain Regimes on Coastal
786 Orographic Precipitation. J. Hydrometeor., 18, 2723–2743, [https://doi.org/10.1175/JHM-](https://doi.org/10.1175/JHM-D-17-0005.1)
787 [D-17-0005.1](https://doi.org/10.1175/JHM-D-17-0005.1), 2017
788
- 789 McMurry, P.H., X.Wang, K.Park, and K.Ehara, The relationship between mass and mobility for
790 atmospheric particles: A new Technique for measuring particle density, Aerosol Sci.
791 Technol., 36, 227–238, 2002
792
- 793 McCoy, D.T., D.L. Hartmann, and D.P. Grosvenor, Observed Southern Ocean Cloud Properties
794 and Shortwave Reflection. Part I: Calculation of SW Flux from Observed Cloud
795 Properties. J. Climate, 27, 8836–8857, <https://doi.org/10.1175/JCLI-D-14-00287.1>, 2014
796
- 797 NOAA, HYSPLIT Trajectory Model, NOAA Air Resources Laboratory, Silver Spring, MD,
798 Accessed 1 August 2016, [Available online at <https://ready.arl.noaa.gov/HYSPLIT.php>],
799 2016
800
- 801 O’Dowd, C.D., M.H. Smith, Physicochemical properties of aerosols over the Northeast Atlantic:
802 evidence for wind-speed-related submicron sea-salt aerosol production, J.Geophys. Res.,
803 98, 1137-1149, 1993
804
- 805 Petters, M. D., J. R. Snider, B. Stevens, G. Vali, I. Faloona, and L. M. Russell, Accumulation
806 mode aerosol, pockets of open cells, and particle nucleation in the remote subtropical
807 Pacific marine boundary layer, J. Geophys. Res. Atmos., 111, 1–15, 2006
808
- 809 Petters, M. D., and S. M. Kreidenweis, A single parameter representation of hygroscopic growth
810 and cloud condensation nucleus activity. Atmos. Chem. Phys., 7, 1961–1971, 2007
811
- 812 Raes, F., R. Van Dingenen, E. Cuevas, P. F. J. Van Velthoven, and J. M. Prospero, Observations
813 of aerosols in the free troposphere and marine boundary layer of the subtropical
814 Northeast Atlantic: Discussion of processes determining their size distribution, J.
815 Geophys. Res., 102, 21315, 1997
816
- 817 Rogers, R. R., and M. K. Yau, A Short Course in Cloud Physics. 3rd ed. Pergamon Press, 304
818 pp., 1989



- 819
820 Romano, A., Applied Statistics for Science and Industry, Allyn and Bacon Inc., pp. 385, 1977
821
822 Schwartz, S.E., Are global cloud albedo and climate controlled by marine phytoplankton?,
823 Nature, 336, 441-445, 1988
824
825 Snider, J.R., D.Leon and Z.Wang, Droplet Concentration and Spectral Broadening in Southeast
826 Pacific Stratocumulus, J. Atmos. Sci., 74, 719-749, 2017
827
828 Tao, W.-K., J.-P. Chen, Z. Li, C. Wang, and C. Zhang, Impact of aerosols on convective clouds
829 and precipitation, Rev. Geophys., RG2001, 2012
830
831 Thompson, G., R.M. Rasmussen and K. Manning, Explicit forecasts of winter precipitation using
832 an improved bulk microphysics scheme. Part I: Description and sensitivity analysis, Mon.
833 Weather Rev., 132, 519 – 542, 2004
834
835 Toon, O.B., The optical constants of several atmospheric aerosol species: Ammonium sulfate,
836 aluminum oxide, and sodium chloride, J. Geophys. Res., 81, 5733 - 5748, 1976
837
838 TSI Inc., accessed 19 December 2018 at:
839 [https://www.artisanng.com/info/PDF__5453495F33373630415F333736325F4461746173](https://www.artisanng.com/info/PDF__5453495F33373630415F333736325F446174617368656574.pdf)
840 [68656574.pdf](https://www.artisanng.com/info/PDF__5453495F33373630415F333736325F446174617368656574.pdf), 1996
841
842 TSI, Inc., Condensation Particle Counter Instruction Manual, St. Paul, Minnesota, 2000a
843
844 TSI, Inc., Model 3080 Electrostatic Classifier Instruction Manual, St. Paul, Minnesota, 2000b
845
846 Twomey, S., Pollution and the Planetary Albedo, Atmospheric Environment, 8, 1251–56, 1974
847
848 Twomey, S., The nuclei of natural cloud formation part II: The supersaturation in natural clouds
849 and the variation of cloud droplet concentration, Geofis. Pura Appl., 43, 243-249, 1959
850
851 van Dingenen, R., A. O. Virkkula, F. Raes, T. S. Bates, A. Wiedensohler, A simple non linear
852 analytical relationship between aerosol accumulation number and sub-micron volume,
853 explaining their observed ratio in the clean and polluted marine boundary layer, Tellus,
854 52B, 439-451, 2000
855
856 Wolfe, J. P., and J. R. Snider, 2012: A relationship between reflectivity and snow rate for a high-
857 altitude S-band radar, J. Appl. Meteor. Climatol., 51, 1111–1128, 2012
858
859 Yum, S. S., and J. G. Hudson, Wintertime/summertime contrasts of cloud condensation nuclei
860 and cloud microphysics over the Southern Ocean, J. Geophys. Res., 109, 1-14, 2004
861



862 Table 1. Aerosol Instruments

Instrument and Reference	Aerosol Property Measured	Particle Diameter Range, μm	Aerosol Flow Rate, $\text{cm}^3 \text{s}^{-1}$	Data Acquisition Rate, Hz	Data Availability (2015)
CPC Model 3010 (TSI 2000a)	Aerosol Concentration	$D > 0.010$	17	1 and 0.1	29 May to 14 Aug
UHSAS (DMT 2013)	Aerosol Size Distribution	$0.055 < D < 1$	0.34	0.1	29 May to 28 June

863

864



865 Table 2. Classification of Air Mass Type

Citation and Location	Measurement Site Characteristics	Air Mass Classification	Averaged CPC Concentration, cm^{-3} ^a
Gras (1990) Cape Grim, Tasmania 40.68 °S; 144.7 °E	Oceanic Wintertime	Remote Marine	100
Brechtel et al. (1998) Macquarie Island (Southwest Pacific) 54.50 °S; 159.0 °E	Oceanic Summertime	Remote Marine	700
Diesch et al. (2012) Portugal 37.11 °N; 7.735 °W	Coastal Continental Late Autumn	Moderately-polluted Marine Heavily-polluted Marine Continental	1000 7000 10000
This Study Arauco, Chile 37.25 °S; 73.34 °W	Coastal Continental Wintertime	Between moderately-polluted Marine and Heavily-polluted Marine	3000
This Study Trinidad Head, CA 41.05 °N; 124.2 °W	Coastal Continental Wintertime	Moderately-polluted Marine	1000

866

867 ^a Values rounded to one significant digit

868


 869 Table 3. Statistics for Onshore Trajectories (D integration in Eq. (2) and (4) is from 0.055 to 1 μm)
 870

Arrival Hour, UTC	Type	Start DDHHMM ^a , UTC	End DDHHMM ^a , UTC	N_{UHSAS} on V_{UHSAS} Slope, μm^{-3}	r ^b	$FAC(D=0.055 \mu\text{m})$	r ^c	Number of Samples
06	Sea Surface	050500	050700	93.	0.54	0.59	0.65	139
12	Sea Surface	051100	051134	64.	0.10	0.19	0.59	63
18	Sea Surface	051700	051900	110.	0.66	0.41	0.63	342
00	Sea Surface	052300	060100	298.	0.81	0.51	0.96	316
06	Sea Surface	060500	060700	60.	0.53	0.18	0.89	677
12	Sea Surface	061100	061300	91.	0.60	0.16	0.65	647
18	Sea Surface	061700	061900	107.	0.33	0.18	0.81	476
00	Sea Surface	062300	062325	234.	0.81	0.36	0.97	133
06	Sea Surface	080500	080700 ^d	163.	0.06	0.29	0.52	542
12	Sea Surface	081100	081300	358.	0.75	0.28	0.76	504
18	Sea Surface	081700	081900	450.	0.88	0.42	0.90	416
00	Sea Surface	090020	090033	764.	0.45	0.34	0.98	72
06	Sea Surface	090500	090700	703.	0.68	0.23	0.96	554
12	Sea Surface	091100	091300	714.	0.89	0.44	0.94	532
18	Sea Surface	091700	091900	675.	0.78	0.39	0.53	592
00	Sea Surface	092300	100100	519.	0.37	0.22	0.68	618
06	Aloft	100500	100700	857.	0.96	0.39	0.82	617
18	Sea Surface	101700	101900	825.	0.86	0.37	0.19	622
00	Sea Surface	110006	110031	834.	0.96	0.50	0.99	61
00	Aloft	262300	270100	420.	0.68	0.47	0.93	647
			<x>	417		0.35		
			σ	297		0.13		
			$\sigma / <x>$	0.71		0.36		

871

872 ^a DDHHMM indicates the start and end times (day in June 2015, hour, minute) of the data segment873 ^b Pearson product moment for the $N_{UHSAS}(D=0.055 \mu\text{m})$ on $V_{UHSAS}(D=0.055 \mu\text{m})$ correlation874 ^c Pearson product moment for the $N_{UHSAS}(D=0.055 \mu\text{m})$ on N_{CPC} correlation875 ^d Data recording ended at DDHHMM = 080646, i.e., 14 min before the stated end time

876 Table 4. Statistics for Onshore Trajectories (D integration in Eq. (2) and (4) is from 0.120 to 1 μm)

Arrival Hour, UTC	Type	Start DDHHMM ^a , UTC	End DDHHMM ^a , UTC	N_{UHSAS} on V_{UHSAS} Slope, μm^{-3}	r ^b	$FAC(D=0.120 \mu\text{m})$	r ^c	Number of Samples
06	Sea Surface	050500	050700	60.	0.74	0.37	0.47	139
12	Sea Surface	051100	051134	40.	0.31	0.12	0.36	63
18	Sea Surface	051700	051900	64.	0.76	0.23	0.49	342
00	Sea Surface	052300	060100	113.	0.84	0.17	0.84	316
06	Sea Surface	060500	060700	34.	0.67	0.10	0.78	677
12	Sea Surface	061100	061300	44.	0.77	0.07	0.42	647
18	Sea Surface	061700	061900	42.	0.61	0.06	0.24	476
00	Sea Surface	062300	062325	107.	0.93	0.15	0.92	133
06	Sea Surface	080500	080700 ^d	89.	0.72	0.12	0.02	542
12	Sea Surface	081100	081300	139.	0.79	0.09	0.53	504
18	Sea Surface	081700	081900	202.	0.92	0.17	0.83	416
00	Sea Surface	090020	090033	184.	0.12	0.06	0.78	72
06	Sea Surface	090500	090700	228.	0.58	0.06	0.87	554
12	Sea Surface	091100	091300	262.	0.92	0.14	0.73	532
18	Sea Surface	091700	091900	257.	0.89	0.12	0.41	592
00	Sea Surface	092300	100100	204.	0.83	0.06	0.32	618
06	Aloft	100500	100700	323.	0.96	0.11	0.82	617
18	Sea Surface	101700	101900	279.	0.91	0.10	0.08	622
00	Sea Surface	110006	110031	346.	0.97	0.16	0.96	61
00	Aloft	262300	270100	171.	0.65	0.18	0.88	647
			< x >	159		0.13		
			σ	100		0.07		
			$\sigma / <x>$	0.63		0.55		

877

878 ^a DDHHMM indicates the start and end times (day in June 2015, hour, minute) of the data segment879 ^b Pearson product moment for the $N_{UHSAS}(D=0.120 \mu\text{m})$ on $V_{UHSAS}(D=0.120 \mu\text{m})$ correlation880 ^c Pearson product moment for the $N_{UHSAS}(D=0.120 \mu\text{m})$ on N_{CPC} correlation881 ^d Data recording ended at DDHHMM = 080646, i.e., 14 min before the stated end time



882

883

884

885

886

887

888

889

890

891

892

893

894

895

896

897

898

899

900

901

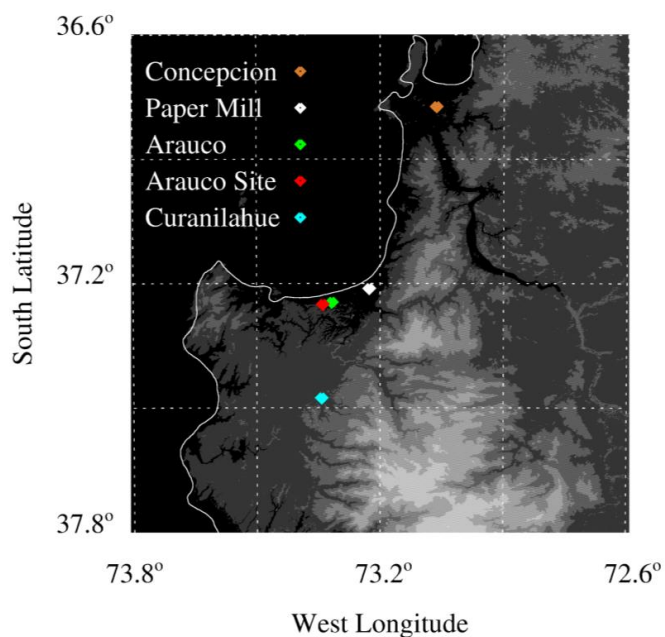


Fig. 1 – Central Chilean Coastal region and the location of Arauco Site where aerosol measurements were made during CCOPE. Altitude thresholds for the digital elevation map are at 0 m MSL, 50 m MSL, 250 m MSL, 500 m MSL, 750 m MSL, and 1000 m MSL.



902

903

904

905

906

907

908

909

910

911

912

913

914

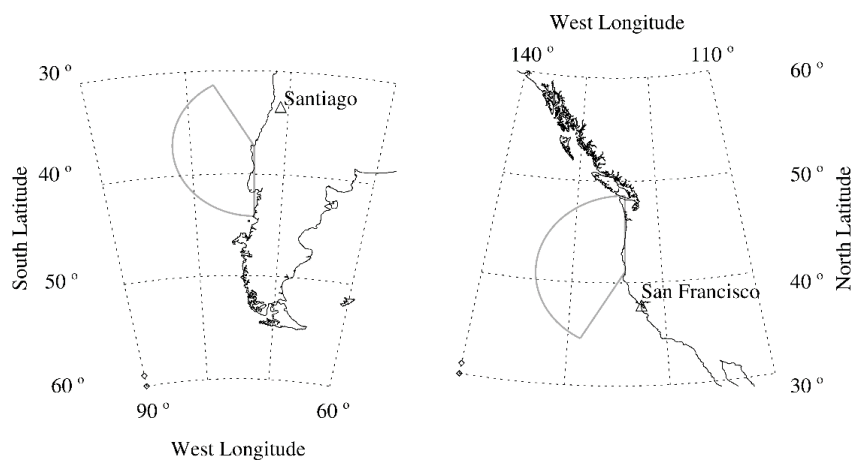


Fig. 2 - Clean sector chosen for Arauco (left, 180° to 330°) and the clean sector chosen for THD (right, 210° to 360°).



915

916

917

918

919

920

921

922

923

924

925

926

927

928

929

930

931

932

933

934

935

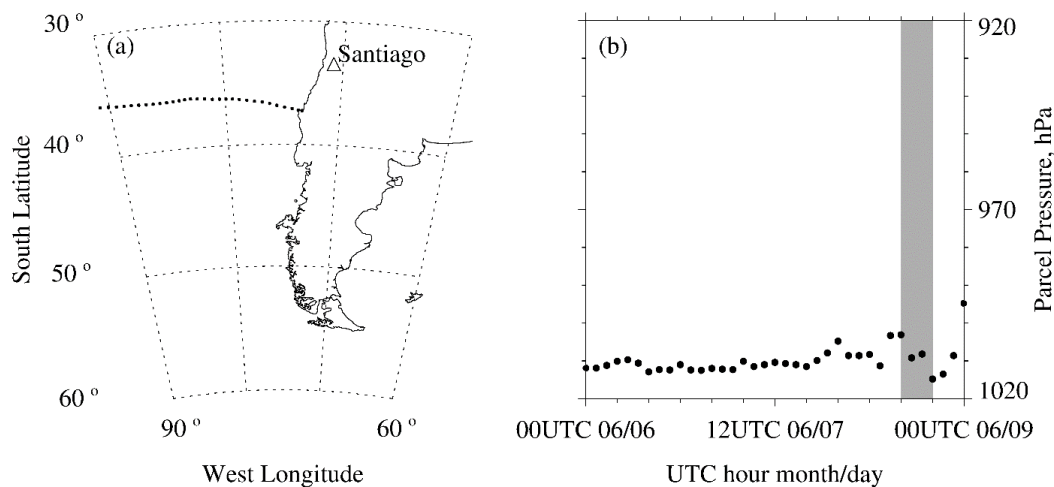


Fig. 3 - a) One of the 18 sea surface trajectories that arrived at the Arauco Site between 29 May to 28 June; this trajectory arrival occurred at 00 UTC June 9. Black dots are hourly output of the HYSPLIT model; however, for clarity, only every other 1-hr point is plotted. b) Hourly HYSPLIT pressure vs time; however, for clarity, only every other 1-hr point is plotted. The averaged sea surface wind speed (U) was evaluated over the 12 to 18 UTC interval show in gray.

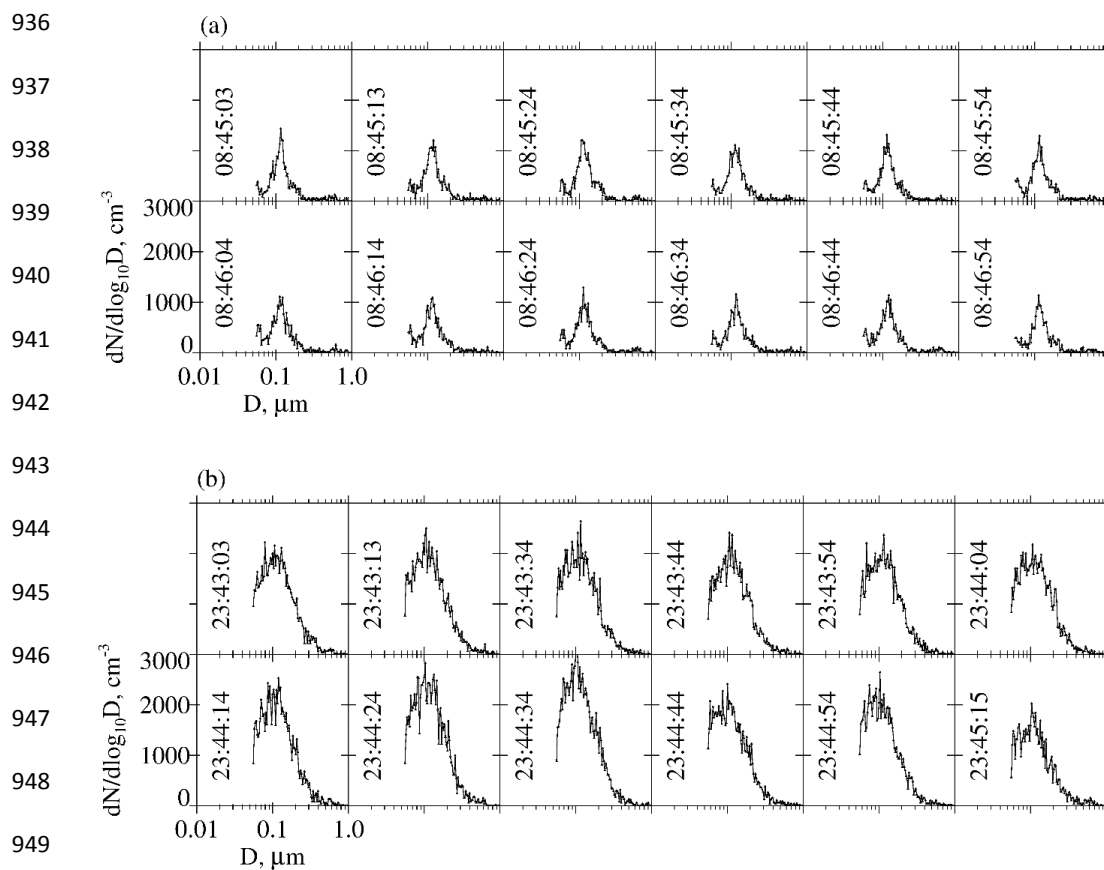
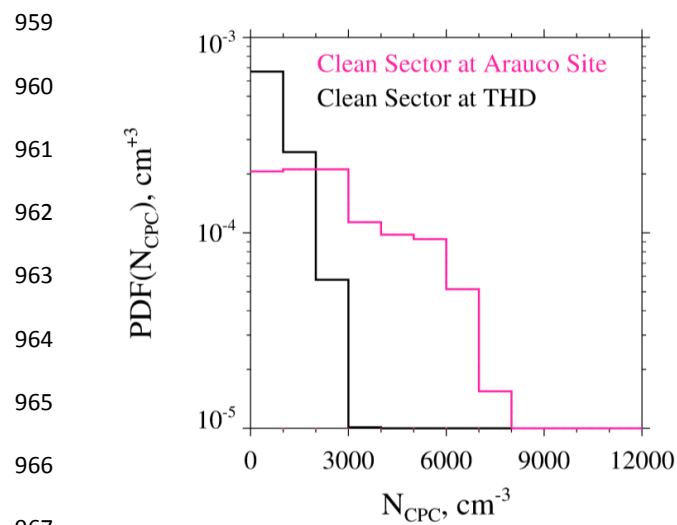


Fig. 4 - Consecutive ASDs recorded by the UHSAS at the Arauco Site. a) ASDs with a relatively small concentration ($\sim 300 \text{ cm}^{-3}$), a right tail of an Aitken mode (at $\sim 0.06 \mu\text{m}$), and an accumulation mode (at $\sim 0.1 \mu\text{m}$), in onshore-moving air on June 5, 2015. b) ASDs with a proportionately larger concentration ($\sim 1100 \text{ cm}^{-3}$), an accumulation mode (at $\sim 0.1 \mu\text{m}$), and no evidence of an Aitken mode, in air thought to be contaminated by continental sources (June 4, 2015). UTC time is written in each panel.



959
960
961
962
963
964
965
966
967
968
969
970
971
972
973
974
975

Fig. 5 - CPC concentration probability distribution functions for the Arauco Site and the THD.

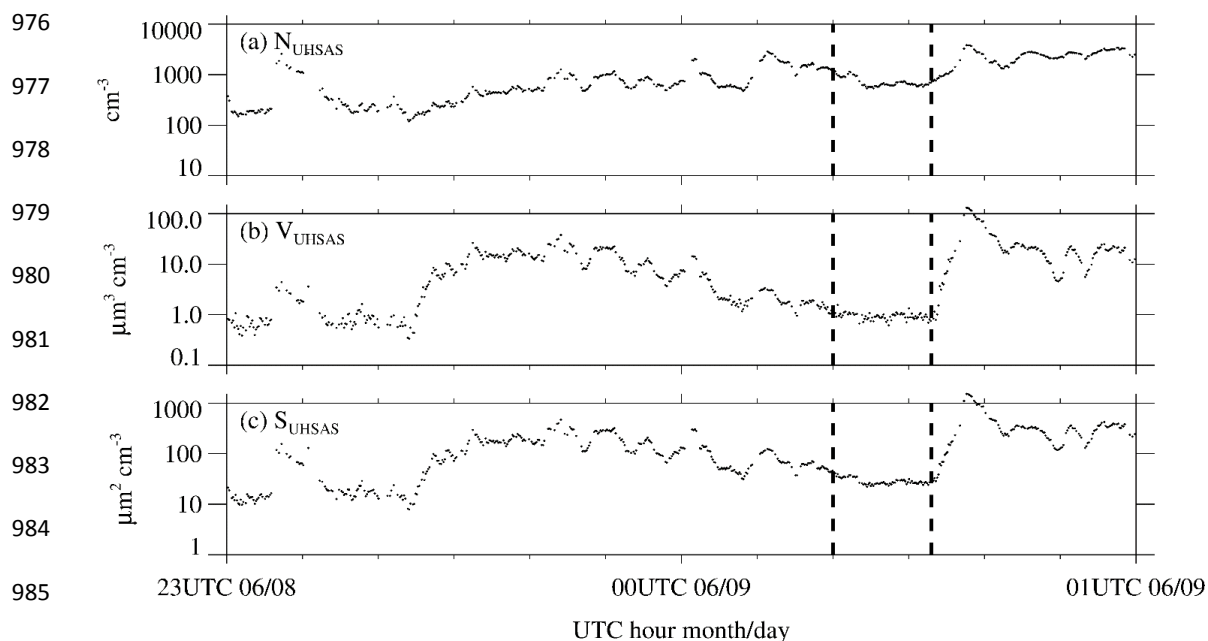
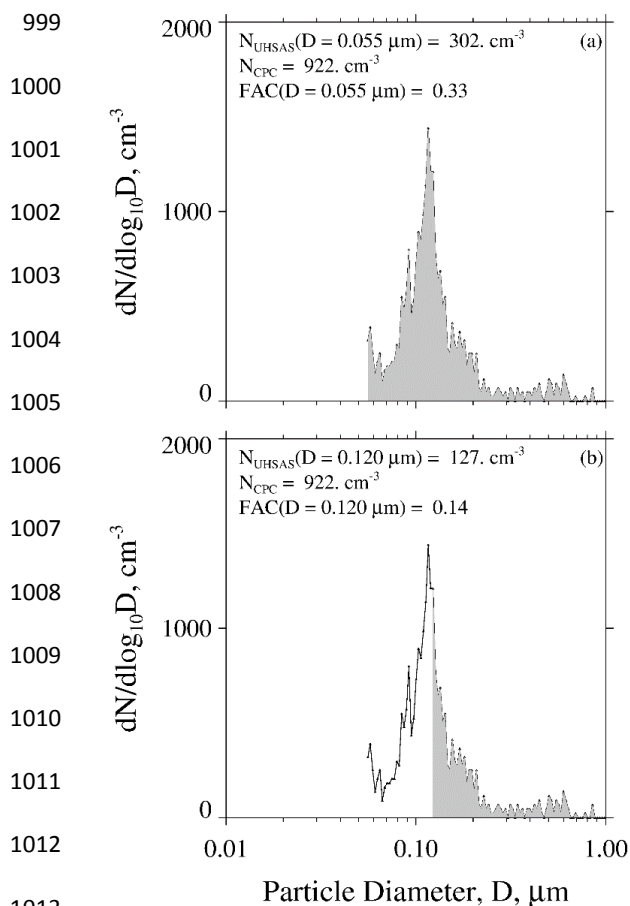


Fig. 6 – Aerosol properties centered on one of the 20 onshore trajectories that arrived at the Arauco Site between 29 May to 28 June. This trajectory arrival occurred at 00 UTC on June 9. a) UHSAS concentration; b) UHSAS aerosol volume; c) UHSAS aerosol surface area. Aerosol properties shown here were filtered using the procedure described in Appendix B. Vertical dashed lines mark the subset of the two-hour segment we picked (subjectively) as being representative of onshore-moving air that was relatively unaffected by continental aerosols compared to adjacent portions of the two-hour segment.



1015 Fig. 7 - Two portrayals of the ASD recorded during CCOPE at 08:45:03 UTC June 5,
1016 2015. This ASD is also plotted in Fig. 4a. Gray area in both panels represents the aerosol
1017 concentration integrated from the indicated lower-limit D to $1 \mu\text{m}$. a) Figure legend has the size-
1018 integrated UHSAS concentration, calculated with lower-limit D set at $0.055 \mu\text{m}$, the CPC
1019 concentration, and the fractional aerosol concentration (FAC). b) Figure legend has the size-
1020 integrated UHSAS concentration, calculated with lower-limit D in Eq. 2 set at $0.120 \mu\text{m}$, the
1021 CPC concentration, and the fractional aerosol concentration (FAC).

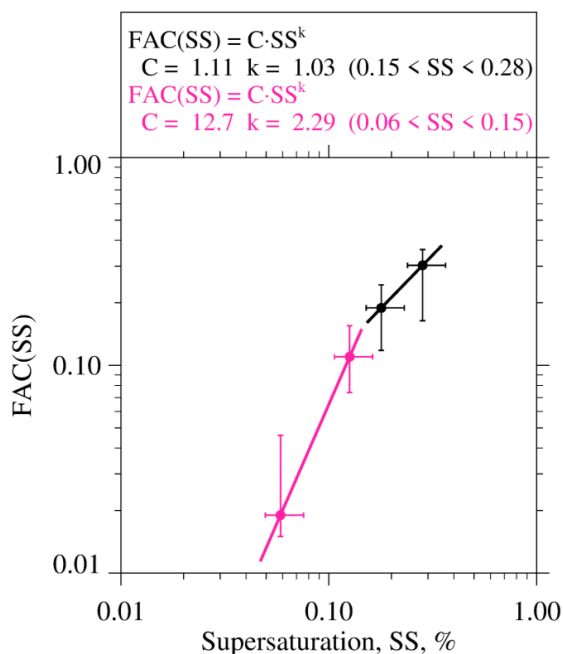
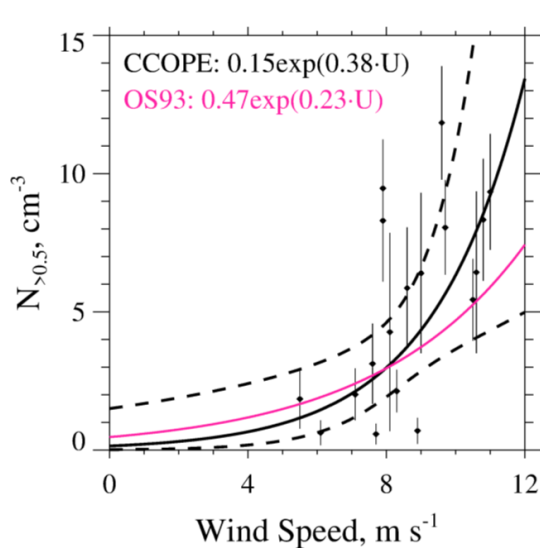


Fig. 8 - Parameterized CCN activity spectrum derived using CPC and UHSAS

measurements from the 20 onshore trajectories that arrived at the Arauco Site between 29 May and 28 June 2015. Pink circles and the pink fit line are for lower-limit diameters set at 0.200 and 0.120 μm . Black circles and the black fit line are for lower-limit diameters set at 0.095 and 0.070 μm . Figure legend has power-law coefficients describing the parameterization; i.e., how *FAC* varies with *SS*.



1053
1054
1055
1056
1057
1058

1059 Fig. 9 – Averaged values of $N_{>0.5}$ (± 1 standard deviation) vs HYSPLIT-derived averaged
1060 U_s for the 18 sea surface trajectories that arrived at the Arauco Site between 29 May and 28 June
1061 2015. The black curve is the fit of the CCOPE data; dashed curves above and below the black
1062 curves are 95% confidence intervals (Romano 1977; his Eq. 4.2.3.f). The pink curve is the fit
1063 reported by O'Dowd and Smith (1993) for $0.38 \mu\text{m} < D < 0.84 \mu\text{m}$.

1064

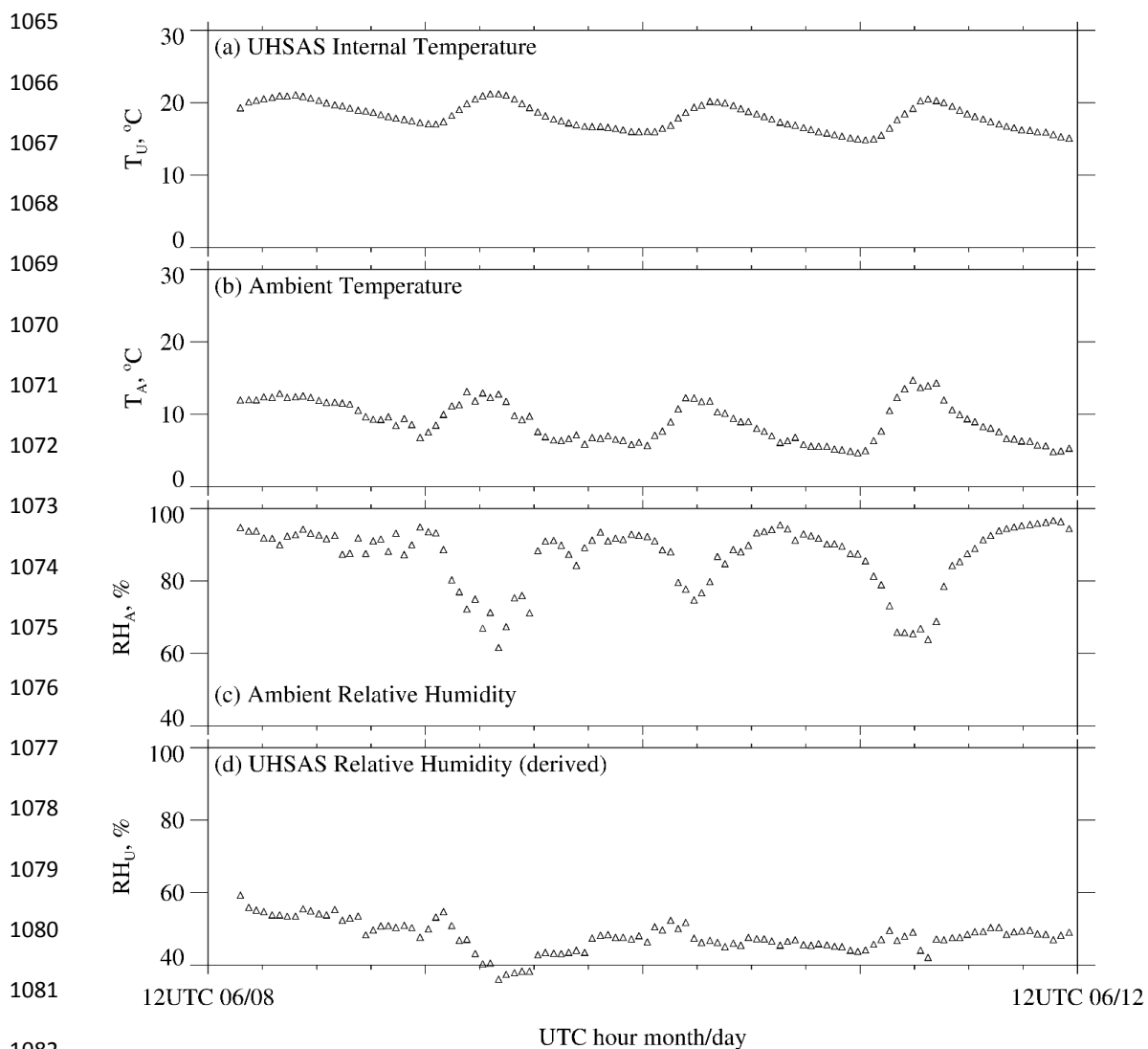


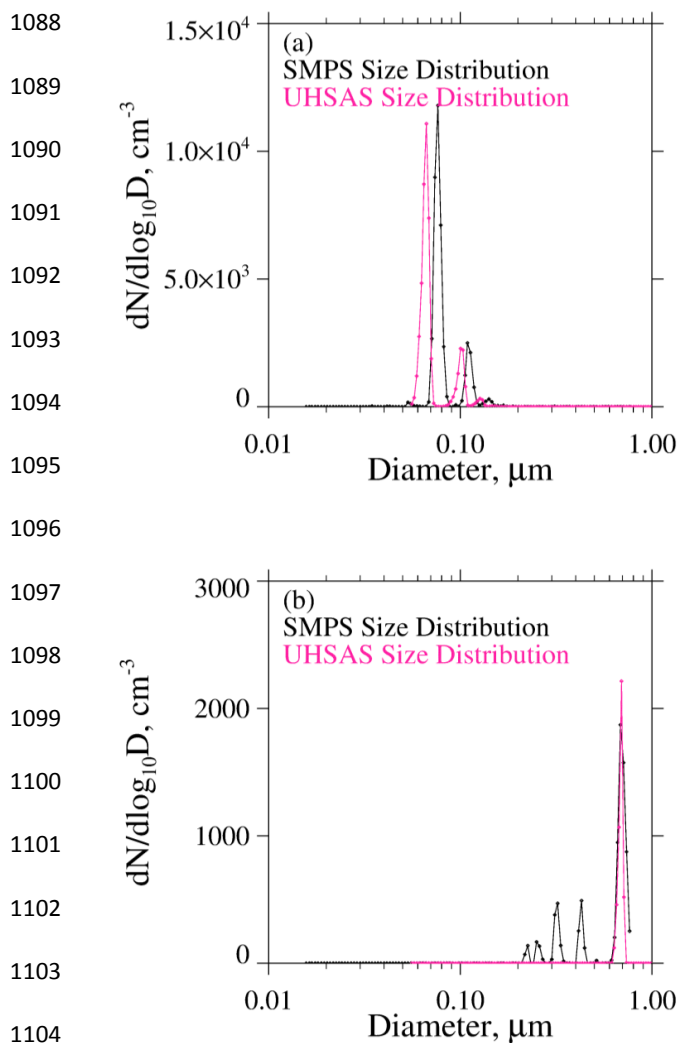
Fig. A1 – UHSAS internal temperature and ambient meteorological parameters at the

Arauco Site over a four day period. a) Temperature inside the UHSAS; b) Temperature measured

on the meteorological tower; c) RH measured on the meteorological tower; d) Derived RH inside

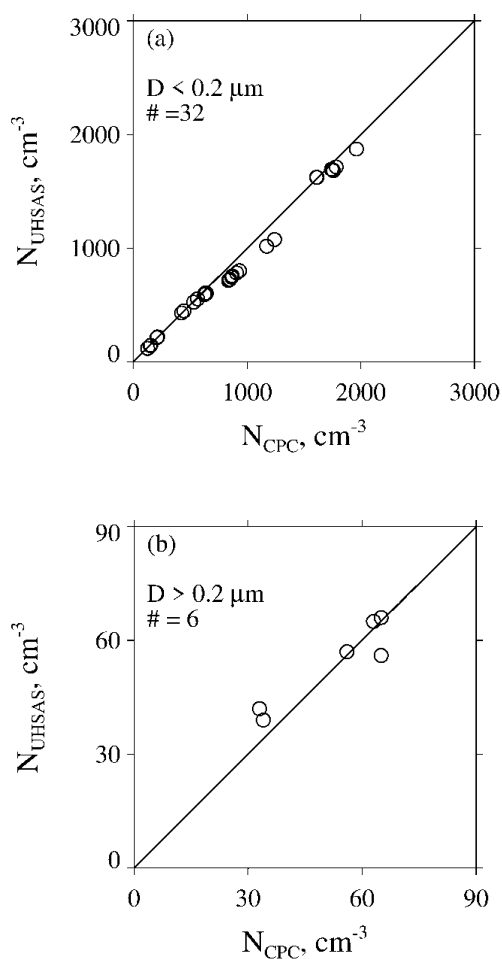
UHSAS.

1087



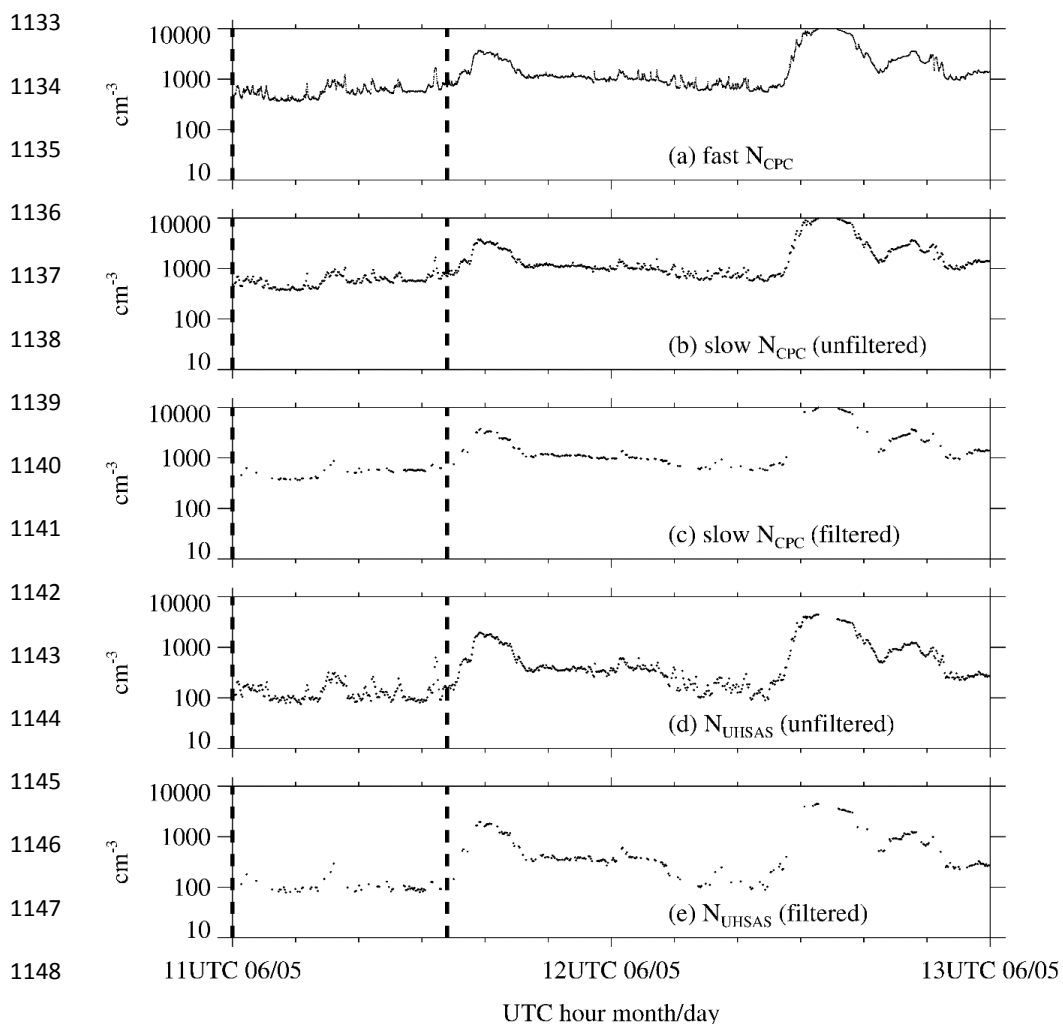
1106 Fig. A2 – a) ASDs corresponding to mobility-selected $D = 0.075 \mu\text{m}$ ammonium sulfate
1107 test particles. b) ASDs corresponding to mobility-selected $D = 0.71 \mu\text{m}$ polystyrene test
1108 particles.

1109



1127 Fig. A3 - a) Size-integrated concentration from by the UHSAS versus concurrent
1128 laboratory measurements of concentration from the CPC. Results are for mobility-selected
1129 ammonium sulfate test particles with $D < 0.2 \mu\text{m}$. b) As in Fig. A3a but for mobility-selected
1130 ammonium sulfate test particles with $D > 0.2 \mu\text{m}$, and for mobility-selected polystyrene latex test
1131 particles with $D > 0.2 \mu\text{m}$.

1132



1150 Fig. B1 - Demonstration of the numerical filter. Measurements from one of the 20
1151 onshore trajectories that arrived at the Arauco Site between 29 May and 28 June. This trajectory
1152 arrival occurred at 12Z June 5. a) 1-s sampled CPC measurements; b) 10-s sampled CPC
1153 measurements; c) filtered 10-s CPC measurements; d) 10-s UHSAS measurements of size-
1154 integrated concentration; e) filtered 10-s UHSAS measurements of size-integrated concentration.
1155